

Experimental and Numerical Analysis of Loss Characteristics of Cooled Transonic Nozzle Guide Vanes

Daniel Burdett

Department of Engineering Science,
University of Oxford,
Oxford OX2 0ES, UK
e-mail: daniel.burdett@univ.ox.ac.uk

Thomas Povey¹

Department of Engineering Science,
University of Oxford,
Oxford OX2 0ES, UK
e-mail: thomas.povey@eng.ox.ac.uk

This article presents high-fidelity experimental traverse measurements downstream of an annular cascade of transonic nozzle guide vanes (NGVs) from a high-pressure (HP) turbine stage. The components are heavily cooled real engine components from a modern civil gas turbine engine, operated at scaled engine conditions. Tests were conducted in the high technology readiness level (TRL) Engine Component Aerothermal (ECAT) facility at the University of Oxford. High-resolution full-area traverse measurements of local kinetic energy (KE) loss coefficient are presented in several axial planes. In particular, we present circumferential loss coefficient profiles at several radial heights, full-area traverses at three axial planes, and fully mixed-out loss calculations. The analysis of these data gives insight into particular loss structures, overall aerodynamic performance, and wake mixing rates. The effect of exit Mach number on performance is also considered. The data address a gap in the literature for the detailed analysis of traverse measurements downstream of HP NGV engine components. Experimental data are compared with steady and unsteady Reynolds-averaged Navier–Stokes (RANS) simulations, allowing benchmarking of typical computational fluid dynamics (CFD) methods for absolute loss prediction of cooled components. There is relatively limited aerodynamic performance data in the literature for heavily cooled NGVs, and this study represents one of the most comprehensive of its type. [DOI: 10.1115/1.4053019]

Keywords: computational fluid dynamics (CFD), fan, compressor, and turbine aerodynamic design, fluid dynamics and heat transfer phenomena in compressor and turbine components of gas turbine engines, heat transfer and film cooling, measurement techniques, turbine blade and measurement advancements, turbomachinery blading design

Introduction

The high-pressure (HP) nozzle guide vane (NGV) plays a significant role in setting the overall engine performance. In particular, the designer must consider the simultaneous optimization of NGV capacity, thermal/cooling performance, and aerodynamic performance. These three factors determine the stage and overall engine operating point. In this article, we consider the aerodynamic performance of heavily cooled parts, tested at nondimensionally representative operating conditions. The importance of this topic is justified by the exchange rate between kinetic energy (KE) loss coefficient and HP turbine stage efficiency: at a typical turbine stage efficiency of 95%, a 1% change in NGV loss coefficient (as a % of loss coefficient) is equivalent to a 0.05% change in HP stage efficiency.

Early attempts to predict turbine stage performance parameters (stage efficiency and losses) primarily involved empirical correlations (e.g., Ainley and Mathieson [1]) or analytical models (e.g., Carter [2]) based on either simplistic linear (and often low speed) cascade tests or data from a bank of engine component tests (loss coefficient and flow angle measurements). These prediction methods were used in turbine design for many decades despite their reliance on extrapolations from overly simplistic experimental correlations, and their increasingly common use in applications with complex geometric features not present in the original test cases. Denton [3] comprehensively reviews methods used to

predict various aspects of loss generation in turbine stages. He warns strongly against relying on correlations obtained from simplified cascade tests in which real engine features were omitted, including 3D vane geometry including lean, sweep, endwall fillets, and endwall contouring; film cooling; realistic trailing edge (TE) geometries with (where relevant) coolant ejection; representative Mach and Reynolds number conditions; representative incident flow turbulence parameters; and realistic surface roughness and surface defects. Instead he advocates for understanding of the fundamental mechanisms of loss generation.

Most of the experimental studies of NGV loss in the open literature have been conducted in simplified experiments designed to isolate the impact of particular design features, e.g., film cooling configurations [4–7]; TE coolant ejection [8–11]; TE design [12–14]; fillets at the vane surface-endwall junctions [15–17]; 3D shaping [18–22]; and inlet flow conditions at the combustor–turbine interface [23–25]. Such experiments are well suited to understanding fundamental aspects of design, but poorly suited to characterizing engine parts in a realistic operating environment. This is important for both early-stage design and also computational fluid dynamics (CFD) calibration. Doing so requires the use of *actual* engine components operating at scaled engine conditions (Mach and Reynolds numbers, and coolant-to-mainstream pressure ratio), ideally (because of periodicity effects) in a fully annular cascade.

A handful of studies in the open literature meet some of these requirements [26–30]: These present aerodynamic traverse measurements from either annular sector or fully annular cascades of vanes that are, to varying degrees, representative of typical engine geometries. Some of these cascades were uncooled, and others were designed to study the effects of specific cooling features

¹Corresponding author.

Contributed by the Heat Transfer Division of ASME for publication in the JOURNAL OF TURBOMACHINERY. Manuscript received February 2, 2021; final manuscript received August 17, 2021; published online January 13, 2022. Assoc. Editor: Alexander Tiedemann.

[6,8]. The studies cover a range of exit Mach number conditions from low speed to mildly supersonic. The primary focusses of these studies were as follows: determining realistic secondary flow structures for modern vanes; studying the development of wake profiles and characterizing mixing losses; and understanding the influence of the radial pressure gradient on the development of wakes and secondary flow structures in annular cascades.

Yasa et al. [31] tested an annular sector of cooled engine guide vanes at exit Mach numbers of 0.60 and 0.95. They compared wake characteristics (depth, breadth, and decay rates) between the subsonic and transonic regimes and studied the influence of endwall fillets on secondary flow development.

The importance of unsteady flow phenomena to the evaluation of NGV aerodynamic performance has been shown by Sieverding et al. [8,32] and Melzer et al. [14,33], who demonstrated its central role in determining TE loss and downstream mixing losses, and its sensitivity to TE shape, thickness, coolant slot geometry, and blowing rate. So far as CFD is concerned, unsteady methods (i.e., unsteady Reynolds-averaged Navier–Stokes (URANS) or LES) are therefore generally seen as a minimum requirement for assessing NGV performance.

Léonard et al. [34] compared Reynolds-averaged Navier–Stokes (RANS), URANS, and LES methods applied to a typical turbine blade at high-subsonic Mach number. They illustrate the hierarchy of prediction accuracy among the three methods: RANS gives an estimate of the mean flow field, but URANS or LES are required to properly resolve the TE flow dynamics. LES offers the most accurate prediction of the complex flow, capturing more of the unsteady interaction between the boundary layers and the TE vortex and shock structures.

In this article, we present comprehensive experimental traverse data downstream of a full annulus of engine part NGVs from the high technology readiness level (TRL) Engine Component Aero-thermal (ECAT) facility at the University of Oxford [35]. In particular, we present detailed characterization of the loss of a fully cooled NGV at engine-representative conditions (represented as both local loss coefficient distributions and average loss coefficient values); axial development of the wake profile; and the effect of Mach number on loss. We also consider the limitations of CFD methods (steady and time-averaged unsteady RANS simulations) for accurate prediction of loss.

Overview of Experimental Facility

Experiments were conducted in the Oxford ECAT facility [35]. This is a high-TRL blowdown facility with a full-annular cascade of engine parts (typically HP NGVs) operated at nondimensionally engine-representative conditions of Mach number, Reynolds number, and coolant-to-mainstream total pressure ratio. Kirolos et al. [35] provide further details of the facility operation and demonstrate the capabilities of the facility for making capacity, aerodynamic loss, and metal effectiveness measurements. The tests presented here used HP NGVs from a large, modern civil turbofan engine. The operating conditions are summarized in Table 1.

A simplified axisymmetric cross section through the ECAT facility working section is shown in Fig. 1. The upstream measurement

plane is located three axial chord lengths upstream of the leading edge plane. The vane exit flow passes into a constant-area duct extending three axial chord lengths downstream of the TE plane, before exhausting into the downstream plenum. Traverse measurements were made in three different axial planes located $\frac{1}{4}$, $\frac{1}{2}$, and $\frac{3}{4}$ of an axial chord length downstream of the TE. These planes are referred to as planes 1, 2, and 3, respectively, as shown in Fig. 1.

The ECAT facility can be operated in two different modes: *blow-down* mode and *regulated* mode [35,36]. These modes achieve varying and steady-state vane exit Mach number conditions during a run, respectively. The area-survey data for this study were collected in regulated mode operation, i.e., at a single, steady operating condition. This can be maintained, with almost no deviation from the target vane pressure ratio ($p_2/p_{0m}=0.55$), for a typical duration of 35 s. Vane exit hub and case static pressure-to-upstream total pressure ratios are shown for a typical regulated run in Fig. 2(a). The normalized mean pressure ratio is also plotted. During the period of 30–65 s, the rms fluctuation about the target value was 0.17%, showing very well-controlled test conditions. A small number of blowdown mode tests were also performed to examine the sensitivity of loss coefficient to exit Mach number. The traverse process in each type of test is outlined in the following section.

The vanes are supplied with coolant from the hub and case (see Fig. 1), feeding film cooling holes distributed over the vane suction and pressure surfaces (six suction side (SS) rows and five pressure side (PS) rows), and a TE slot with a suction side overhang of length 13.4% of axial chord. The hub and case coolant flows are independently metered to high accuracy, giving precise control over the mass flows during a run. Typical coolant-to-mainstream pressure ratio characteristics are plotted in Fig. 2(b), showing good control within a tight band (approximately $\pm 0.02\%$ of the target value). It has been established that the coolant capacity characteristic is relatively insensitive to p_{0c}/p_{0m} [36]. The overall mass flowrate variation expected due to this variation is $\pm 0.005\%$ of the target value.

Instrumentation and Measurement Process

Vane upstream total pressure, p_{0m} , was measured using four fixed Pitot rakes, each with eight measurement points distributed across the vane span (i.e., 32 total pressure measurements). Vane exit static pressure was measured on six vanes (from a total of 40) at tapings located on the hub and case platform overhangs approximately 5 mm downstream of the cascade TE plane. These locations are shown in Fig. 1. Each of the six vanes was instrumented with six tapings at the hub and eight at the case (i.e., 84

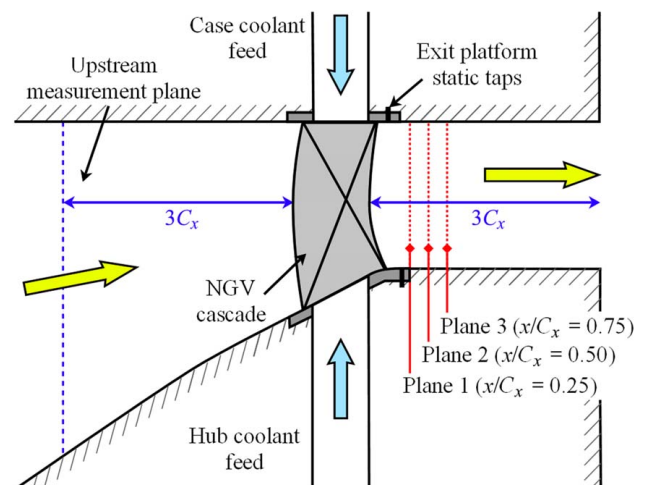


Fig. 1 Axisymmetric cross section schematic of the ECAT facility working section

Table 1 Typical ECAT facility operating conditions

Parameter	Nominal value
Vane inlet total pressure, p_{0m} (bar)	1.85–2.50
Vane pressure ratio, p_2/p_{0m} (–)	0.44–0.78
Vane exit Mach number, M_2 (–)	0.60–1.15
Vane exit Reynolds number, Re (–)	2×10^6 – 8×10^6
Coolant-to-mainstream pressure ratio, p_{0c}/p_{0m} (–)	1.025
TE slot-to-mainstream momentum flux ratio	0.48
Mainstream mass flow, \dot{m}_m (kg/s)	7.8–15.8
Inlet total temperature, T_{01} (K)	280–350
Inlet turbulence intensity, Tu (%)	6–10

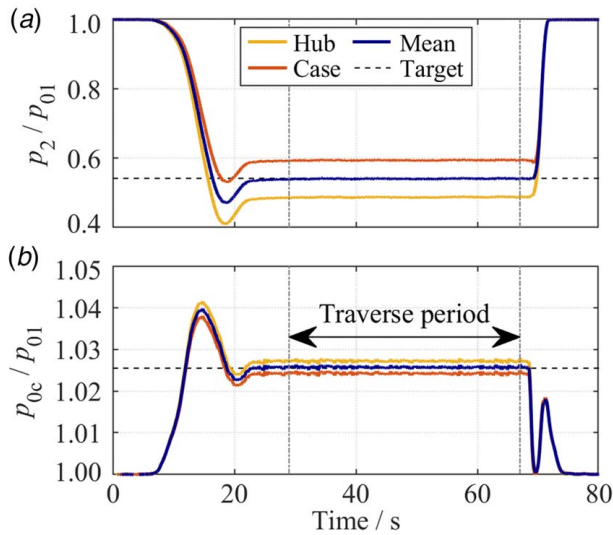


Fig. 2 (a) Vane exit static-to-inlet total pressure ratios and (b) vane coolant-to-mainstream pressure ratios during a typical regulated (steady-state) run

tappings in total). The estimated bias and precision errors in the measurement of operating pressure ratio were $\pm 0.365\%$ and $\pm 0.007\%$, respectively, to 95% confidence. A detailed uncertainty analysis is presented in Ref. [36].

Traverse measurements were conducted using a two-axis (radial-circumferential) hub-mounted traverse gear, capable of traversing the entire annulus in a series of 40 deg sectors. The traverse equipment is described in Ref. [35]. Measurements were conducted using a five-hole pneumatic pressure probe (tip diameter 2.8 mm) calibrated over the range of Mach numbers $0.3 \leq M \leq 1.4$. This allowed determination of total and static pressures, Mach number, and pitch and yaw angles. A single-hole Pitot probe was used very close to the hub and case endwalls. Photographs of the probe tips are shown in Fig. 3.

Area surveys were conducted in *regulated mode* at a nominal exit Mach number $M_2 = 0.97$, with typical variation of $\pm 0.14\%$ of the target value. These were performed over a circumferential range of 2.5 vane pitches (covering two complete vane wakes) and a radial range as close to the complete span as was practically possible (around 3–97% of span). The circumferential limits in each of the three traverse planes were carefully set to measure wakes from the same two vanes in each case. This is demonstrated schematically in Fig. 4. A full-area survey required six runs of the facility and a total of 50–60 circumferential passes of the traverse probe in alternating circumferential directions at different radii. The radial step size was approximately 1.4 mm. The resulting traverse pattern is illustrated in Fig. 5. Alternating line weights indicate the six individual runs. The two sections immediately adjacent to the hub and case boundaries were surveyed with the Pitot probe.

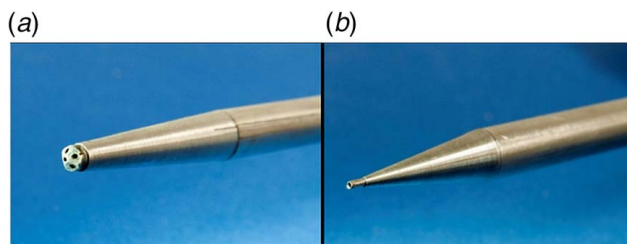


Fig. 3 Photographs of the traverse probe tips: (a) five-hole probe and (b) pitot probe

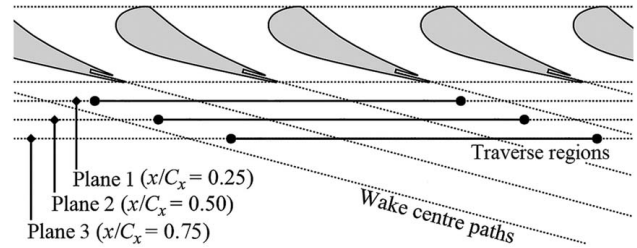


Fig. 4 Schematic of experimental traverse planes and circumferential limits

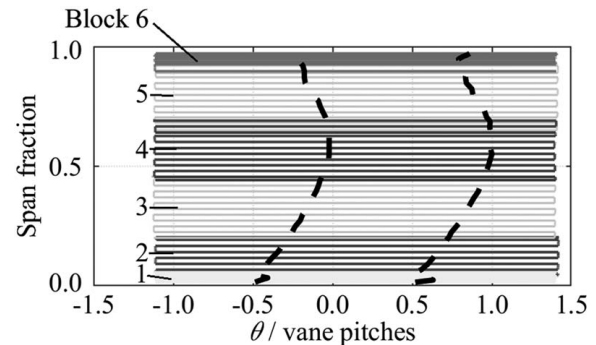


Fig. 5 Typical traverse pattern for a steady-state area survey, showing six individual traverse sections. NGV wake locations are marked by bold dashed lines.

Midspan circumferential traverses were conducted in blowdown mode, the probe being continuously traversed back and forth at midspan, while the exit Mach number falls slowly through the range $1.15 > M_2 > 0.60$. The traverse pattern (composite of two runs: see overlapping lines) is illustrated in both (θ, r) -space and (θ, M_2) -space in Fig. 6. Midspan circumferential traverses were conducted in the same three axial planes as the area surveys and over the same circumferential ranges (see Fig. 4).

The probe-transducer measurement system was experimentally [37] and theoretically [38] determined to have a frequency response of 120 Hz. At a traverse speed of 9.0 deg/s (approximately 58.3 mm/s at midspan), this is equivalent to an effective spatial resolution of 0.49 mm. The impulse response deconvolution technique presented by Burdett et al. [37] was employed to improve the system frequency response—with almost no loss of fidelity of underlying signal—to approximately 720 Hz, or a spatial resolution of 0.08 mm (at midspan). In the impulse response technique, the inverse impulse response function (i.e., the transfer function that takes the measured signal as its input (filtered by the probe-transducer system) and outputs the underlying “true” signal) is approximated for the probe-transducer system and applied as a digital filter to the measured pressure signal. This technique will be familiar to the heat transfer community where it is commonly used to extract transient heat flux signals from a measured temperature history. For area surveys with a traverse pattern made up of alternating sweep directions (Fig. 5)—almost universal—it is necessary to have adequate frequency response to avoid apparent spatial discontinuities at sharp gradients in the underlying flow. That is, inadequate system frequency response causes apparent circumferential offsets in alternating sweeps of the traverse (space-time transformation effect).

Numerical Methods

Steady and unsteady 3D RANS simulations were performed using ANSYS CFX. The 3D domain is shown in Fig. 7. Two

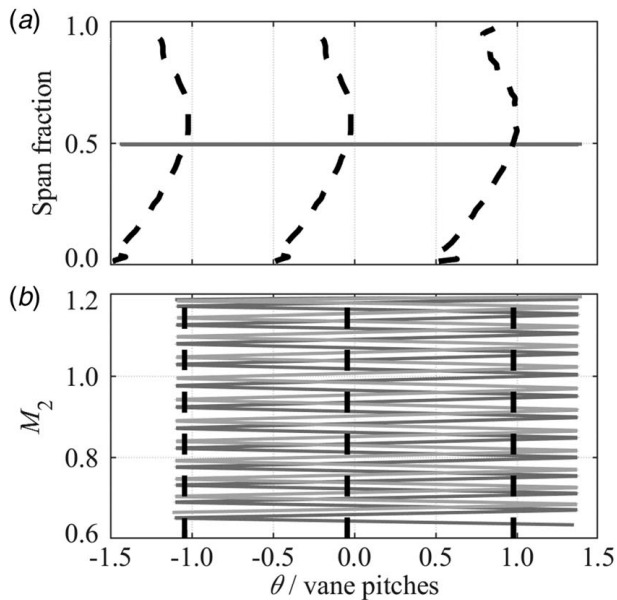


Fig. 6 Typical traverse patterns for a blowdown midspan circumferential traverse: (a) in (θ, r) -space and (b) in (θ, M_2) -space, showing two runs. Wake locations are marked by dashed lines.

vane passages were meshed, with rotational periodicity. The solid boundaries were set as adiabatic walls. The NGV geometry was engine representative, but with different treatment of the film cooling holes in different simulations—as will be described. The mesh was octree based, generated using BOXERmesh. A midspan cross section through the mesh is shown in Fig. 8. Fine mesh refinement was concentrated close to the vane TE, with moderate mesh refinement following the expected path of the vane wakes. A grid sensitivity study was conducted to ensure the results were grid independent, using three grids with cell counts of approximately 18 M, 33 M, and 57 M cells. Grid independence was assessed using a range of metrics including vane capacity, and radial and circumferential distributions of velocity, static, and total pressure. The finest of the three meshes (57 million cells) was used for the study in this article.

Uniform conditions of total pressure and temperature were specified at the inlet boundary, matched to nominal experimental conditions (Table 1). At the exit boundary, an area-average static pressure was set to match the design vane exit Mach number. The radial and

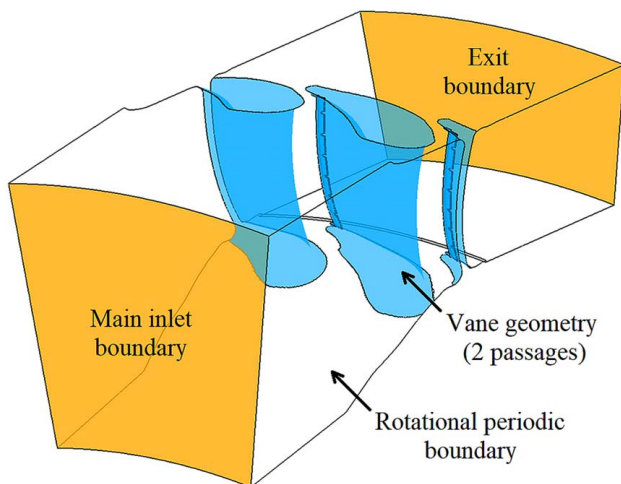


Fig. 7 Geometry for CFD simulations

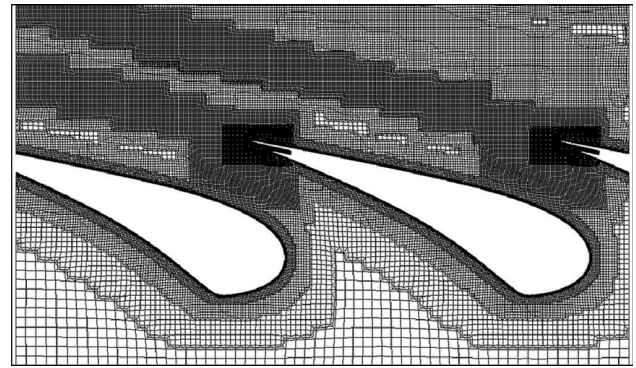


Fig. 8 Section through the mesh at midspan

circumferential exit static pressure distributions were unconstrained, but with the condition that radial equilibrium was satisfied. To ensure precise comparisons of exit Mach number between experiments and CFD, the static pressure field in the CFD solutions was interrogated at the locations of the *experimental* tappings on the hub and case vane exit platforms. The specified average static pressure at the CFD exit boundary was adjusted by trial-and-error until the mean static pressure across the tapping locations (14 locations for one vane pair) was matched with the value measured in the experiment.

The modeling of the TE slot is illustrated in Fig. 9. The coolant flow inlet boundary was located eight slot thicknesses upstream of the slot exit plane. The slot was segmented into seven distinct sections in the spanwise direction by six internal ribs. The rib geometry was modeled on the engine component, with fully resolved elliptical TEs. This allowed realistic development of the coolant flow before exiting into the mainstream flow and therefore aims to achieve realistic prediction of nonuniform coolant flow distribution at the slot exit. A mass flow boundary condition was set over the inlet boundary as a whole, with the solver free to determine the distribution over the individual boundary faces.

The solver settings were second-order discretized and density based. The $k-\omega$ shear stress transport (SST) model was used for turbulence closure (hybrid model, with $k-\epsilon$ formulation in the free-stream, and $k-\omega$ model in inner boundary layer regions), a popular choice for simulations of complex 3D vane geometries. Further details of the numerical setup are provided in Ref. [39].

To understand the requirements of CFD for accurately predicting loss, three different types of numerical simulations were run, with increasing sophistication, as follows:

Simulation 1: Steady RANS simulations without film cooling but with TE slot flow. These were intended to help separate the effects of film cooling by first studying the underlying flow and also to aid in understanding the impacts of smaller features that can be obscured by the film flows.

Simulation 2: Steady RANS simulations with film cooling flows modelled using a point-source model. In these simulations, additional mass flows (specified as fractions of the mainstream mass

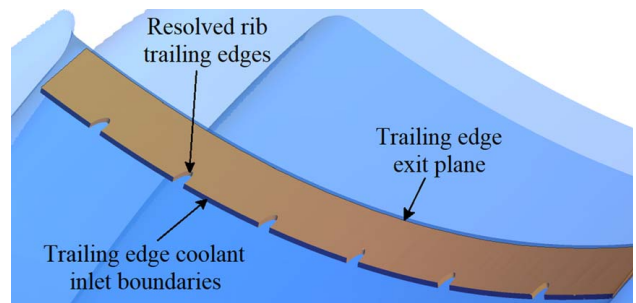


Fig. 9 Detail of TE slot internal cooling geometry

flow) and associated direction vectors were added to the continuity equation at the vane surface locations corresponding to every film cooling hole exit on the physical part. Individual row mass flowrates were determined from the coolant system design data for the component and scaled to match the total coolant capacity measured in the experimental facility. The mass flow split between individual holes in a particular row was estimated using a simple model based on local exit static pressures (evaluated using a pressure field from uncooled simulations) and feed total pressure.

Simulation 3: Unsteady RANS simulations with point-source film cooling. These simulations were initiated from the converged steady RANS results. The time-step was set to one tenth of the estimated TE vortex shedding period. Simulations progressed until the equation residuals were converged to within 10^{-6} , and the values at strategically placed monitor points in the wake region had converged to essentially periodic fluctuations. Time-averaged solutions were then evaluated over 20 shedding periods. The Strouhal number associated with unsteady fluctuations, based on the TE diameter and the free-stream exit velocity, was 0.27, equivalent to a shedding frequency of 43.6 kHz. It was evaluated at three points along the vane span and found to be radially invariant to within 8%.

Definitions of Loss Coefficient

We denote loss using a KE loss coefficient, ζ , expressed in terms of total and static pressure:

$$\zeta = 1 - \frac{1 - \left(\frac{p_2}{p_{02}}\right)^\chi}{1 - \left(\frac{p_2}{p_{01}}\right)^\chi} \quad (1)$$

where $\chi = (\gamma - 1)/\gamma$. Detailed discussion of the suitability of this definition is provided in Appendix A. The analysis presented in this article considers a series of different representations of losses: local distributions in a particular axial plane, radial distributions of circumferentially averaged loss coefficient, average values in a particular axial plane, and fully mixed-out loss coefficient values. In each of these cases, we settle on a slightly different practical definition of loss coefficient. The rationale through which each of these was reached is presented in Appendix A, but the final definitions are repeated here for clarity.

A local kinetic energy loss coefficient is defined at every point in the flow by

$$\zeta'(r, \theta) = 1 - \frac{1 - \left(\frac{p_2(r, \theta)}{p_{02}(r, \theta)}\right)^\chi}{1 - \left(\frac{p_2(r, \theta)}{p_{01}}\right)^\chi} \quad (2)$$

where $p_2(r, \theta)$ and $p_{02}(r, \theta)$ are measured in the plane of interest, and p_{01} and T_{01} are assumed uniform. The circumferential-average loss coefficient at a particular radial height is defined as follows:

$$\zeta'''(r) = 1 - \frac{1 - \left(\frac{\overline{p_2}(r)}{\overline{p_{02}}(r)}\right)^\chi}{1 - \left(\frac{\overline{p_2}(r)}{p_{01}}\right)^\chi} \quad (3)$$

where $\overline{p_2}(r)$ is the circumferentially area-averaged static pressure and $\overline{p_{02}}(r)$ is the circumferentially mass flux-averaged total pressure. The average loss coefficient for an entire 2D plane is

defined by

$$\zeta'''' = 1 - \frac{(\dot{m}_m + \dot{m}_c) \left[1 - \left(\frac{\overline{p_2}}{\overline{p_{02}}}\right)^\chi \right]}{\dot{m}_m \left[1 - \left(\frac{\overline{p_2}}{p_{01}}\right)^\chi \right] + \dot{m}_c \left[1 - \left(\frac{\overline{p_2}}{p_{0c}}\right)^\chi \right]} \quad (4)$$

where $\overline{p_2}$ and $\overline{p_{02}}$ are the plane area-averaged static pressure and plane mass flux-averaged total pressure, respectively, and \dot{m}_m and \dot{m}_c are the mainstream and coolant mass flowrates. Finally, the mixed-out KE loss coefficient is defined by

$$\zeta''''' = 1 - \frac{(\dot{m}_m + \dot{m}_c) \left[1 - \left(\frac{\overline{p_2'}}{\overline{p_{02}'}}\right)^\chi \right]}{\dot{m}_m \left[1 - \left(\frac{\overline{p_2'}}{p_{01}}\right)^\chi \right] + \dot{m}_c \left[1 - \left(\frac{\overline{p_2'}}{p_{0c}}\right)^\chi \right]} \quad (5)$$

where $\overline{p_2'}$ and $\overline{p_{02}'}$ are the mixed-out values of static and total pressure, respectively, evaluated using the method of Dzung [40].

Experimental and Computational Results

The experimental and computational results are now considered. We begin by analyzing local distributions of KE loss coefficient in three axial planes.

Local Kinetic Energy Loss Coefficient Distributions. Full-area experimental surveys of local KE loss coefficient, ζ' (Eq. (2)) in planes 1, 2 and 3 are shown in Figs. 10(a)–10(c), for a vane exit Mach number $M_2 = 0.97$. Corresponding time-averaged URANS-predicted ζ' distributions (i.e., simulation 3) in the same three axial planes (planes 1–3) are shown in Figs. 10(d)–10(f). The time-average was computed over 20 vortex shedding periods, equivalent to an averaging period of 4.6×10^{-4} s. The data are viewed from downstream to upstream (PS to the left of the wake and SS to the right, as shown in Figs. 10(a) and 10(b)).

First consider the experimental data, starting with plane 1 (Fig. 10(a)). The wake signature is curved, in line with the *compound lean* in the aft chord region of the vane (see Fig. 7). The peak value of ζ' in the wake center is higher close to the hub, corresponding with a higher average local surface Mach number. There are also a series of distinct peaks along the line of the wake, separated by loss coefficient minima. This pattern corresponds with the nonuniform coolant ejection from the TE slot (see Fig. 9).

Secondary flow loss cores can be seen at the junctions between the wakes and the hub endwall, but no clear secondary loss cores are visible at the case. This difference is attributed to the influence of the radial pressure gradient, which stimulates radial migration of low-momentum flow toward the hub (causing accumulation and keeping secondary cores close to the wall) and away from the case (causing rapid dispersal of secondary cores). We examine this effect in more detail in the discussion related to Fig. 11.

Moving downstream to planes 2 (Fig. 10(b)) and 3 (Fig. 10(c)), the peak values of ζ' successively drop in magnitude, and the wakes broaden in width, as the flow gradually mixes out. This axial development is examined in more detail in the analysis of Figs. 19–23. The flow field becomes increasingly uniform, both radially and circumferentially. The distortion of the characteristic bowed shape of the wake becomes increasingly exaggerated due to the action of secondary flows induced by the momentum disparity between the high-loss wake and low loss passage flow. The overall details of the data are fairly exceptional for experimental measurements of engine hardware.

Consider now the difference between the experimental and numerical data in equivalent planes. URANS performs well in reproducing the general wake shapes, as well as the difference in endwall boundary layer thickness and secondary flow intensity between hub and case. The peak values of ζ' in the wake center are greater in CFD than in experiment, and the wakes are narrower.

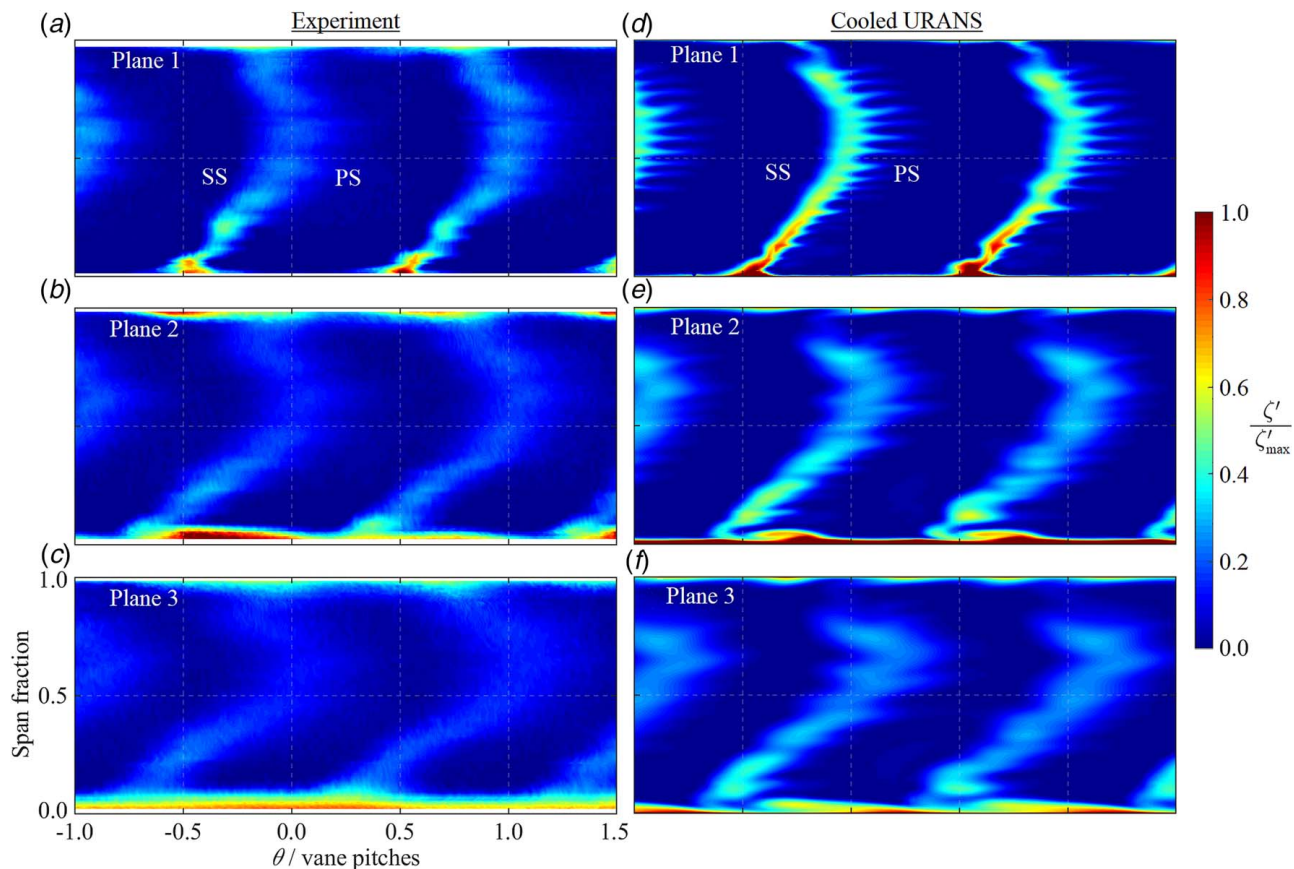


Fig. 10 Local distributions of KE loss coefficient, ζ' , from experiment and cooled URANS in planes 1, 2, and 3

This stems from the well-known weakness of many CFD methods in predicting the rate of mixing due to inadequate turbulence modelling. A particular manifestation of this effect can be seen in the horizontal striations to the PS (right-hand side) of the wakes in Fig. 10(d). These features represent individual film flows from the rear-most PS row (74% tangential chord), which are significantly undermixed when compared to the experimental data. The general development of the CFD-predicted flow field between the three planes is very similar to the experimental data, but always undermixed in comparison.

We now examine the secondary flow regions in detail. Close-up views of these regions in plane 1 at both hub and case are shown in Fig. 11 for experiment, cooled RANS, and time-averaged cooled URANS. Consider first the case regions (Figs. 11(a)–11(c)). The case secondary flows are significantly less intense than at the hub. This is due to a combination of lower Mach numbers and spreading of the loss caused by downwash due to the radial pressure gradient.

The CFD cases differ from the experiment in that the near-wall loss core (marked A in frames a, b, and c) and the wake loss region (marked B in frames a, b, and c) are separated by a region of low loss coefficient, as opposed to being joined. This is likely the result of overprediction of the downwash effect within the low-momentum boundary layer region as a secondary consequence of undermixing of the near-wall flow with the main flow. This effect is even greater in cooled URANS, with the wake loss region beginning at around 90% span as opposed to 93% in cooled RANS.

In CFD, specific secondary loss cores are identified by inspection of 3D flow structures with significant streamwise vorticity. The vortex identification parameters proposed in Ref. [41] were used for this purpose. In both CFD cases, the case passage vortex loss core (the PS leg of the leading edge horseshoe vortex) is located on the SS of the wake at the outer edge of the wake loss region (marked C in frames b and c, with the rough core boundary indicated

by a dashed white line). This core is identified by having negative vorticity (clockwise rotation when viewed from downstream). No passage vortex core can be distinguished in the experimental data, being largely mixed out even at plane 1. Underprediction of mixing is the likely cause of stronger secondary flows in CFD compared to the experimental data, while overprediction of inlet boundary layer thickness is a possible additional contributing factor.

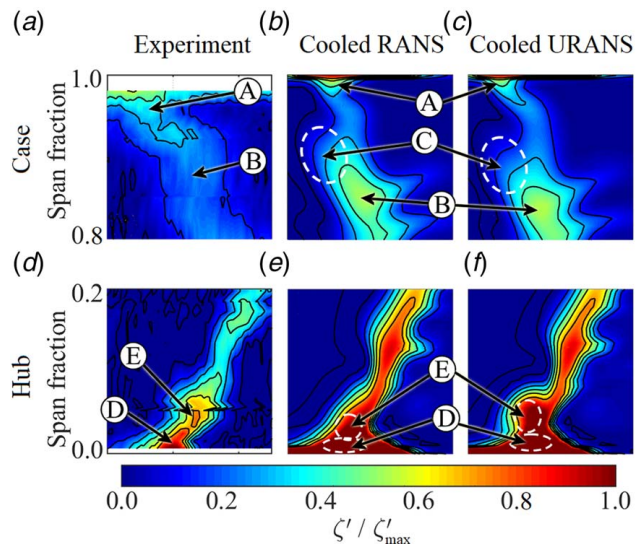


Fig. 11 Comparison of (a)–(c) case, and (d)–(f) hub, secondary loss cores among experiment, cooled RANS, and cooled URANS

We now turn to the hub regions (Figs. 11(d)–11(f)). Two distinct secondary loss cores can be seen in the experimental data (frame d): a larger, high intensity core at approximately 2% span (marked D in frame d) and a smaller, lower intensity core at approximately 7% span (marked E in frame d). These two cores likely correspond with the PS (passage vortex) and SS legs of the leading edge horseshoe vortex, respectively.

In the two CFD cases (frames e and f), the same loss cores D and E can be seen within a larger hub secondary loss core. We can identify them as likely originating from the PS and SS legs of the leading edge horseshoe vortex by confirming that they have positive and negative vorticities, respectively. The PS leg (core D) lies flat on the hub endwall, with the SS leg (core E) just above it at around 5–7% span. The rough locations of the two individual cores are indicated by dashed white lines. The shape of core E differs between cooled RANS and URANS, having greater protrusion to the SS of the wake in frame f.

Spanwise Variation in Circumferential Profiles of Local Kinetic Energy Loss Coefficient. In Fig. 12, we plot circumferential profiles of ζ' at 75%, 50%, and 25% span, in each of planes 1–3. Each profile is radially averaged over $\pm 5\%$ span at each location to reduce sensitivity to individual coolant films. As expected, at all three spanwise locations, we see the wake profiles mix out in the downstream direction (moving between planes 1 and 3) with an incremental reduction in peak loss coefficient in the wake center and an increase in wake width. We consider the decay rate of peak loss coefficient and the growth of the wake width in the analysis of Figs. 19–23.

The wake profiles are quasi-normal in distribution, with a slight asymmetry: the gradient of ζ' is steeper moving away from the SS of the trailing edge than from the PS. This is despite the SS boundary layer at the trailing edge being approximately five times thicker than the PS boundary layer based on CFD-predicted displacement thicknesses (gradual diffusion on the late SS with some shock–boundary layer interaction, compared to rapid acceleration on the late PS). The wake region is—of course—more complex than simply the confluence of the two surface boundary layers, featuring two distinct trailing edge *base regions* with different associated base

pressures. Coolant flow ejects from the trailing edge slot into the cutback region upstream of the SS TE, reducing the gradient on the PS of the wake.

We now compare the measured circumferential profiles of local KE loss coefficient *between* spanwise locations. The results at 75% and 50% span are very similar. In plane 1, the peak heights differ by just 6.7% and the wake widths (defined as the range over which ζ' exceeds 50% of the peak value) by 6.5%. At 25% span, however, the peak losses are notably higher. Comparing to 50% span data, the peak loss coefficient values at 25% span are higher by +36.3%, +35.4%, and +30.9% in planes 1, 2, and 3, respectively. The difference is primarily due to spanwise variation of the axial location of the vane TE with respect to the traverse plane: the test vane has moderate positive compound lean and sweep such that the hub and case sections are further axially downstream (hub more so than case) than the midspan section. Thus, the near-hub wake is undermixed with respect to other vane sections at a particular traverse plane, an effect that is more pronounced at plane 1 than further downstream.

Axial Variation in Circumferential Profiles of Local Kinetic Energy Loss Coefficient. In Fig. 13, we compare the axial development of midspan circumferential profiles of ζ' from experiment and from the three different CFD cases (steady cooled, steady uncooled, and unsteady cooled).

The most striking feature of the comparison is the significant overprediction of loss and underprediction of mixing in all of the CFD simulations. This is true in all three axial planes. Broadly speaking, the predicted *peak* loss (due to both overprediction of overall loss and undermixing of the wake) is approximately double that measured experimentally. This is a fairly significant result for multirow analysis: in our particular example, a rotor leading edge would typically sit in the range $0.30 < x/C_x < 0.60$, and all three CFD methods would grossly overpredict the arising unsteadiness and forcing function.

We now compare the three CFD methods. Adding film cooling to the steady simulation has two effects. First, a small (around 3–5%) increase in peak loss (expected due to the thicker boundary layers) and second, a broadening of the PS edge of the wake profile (by

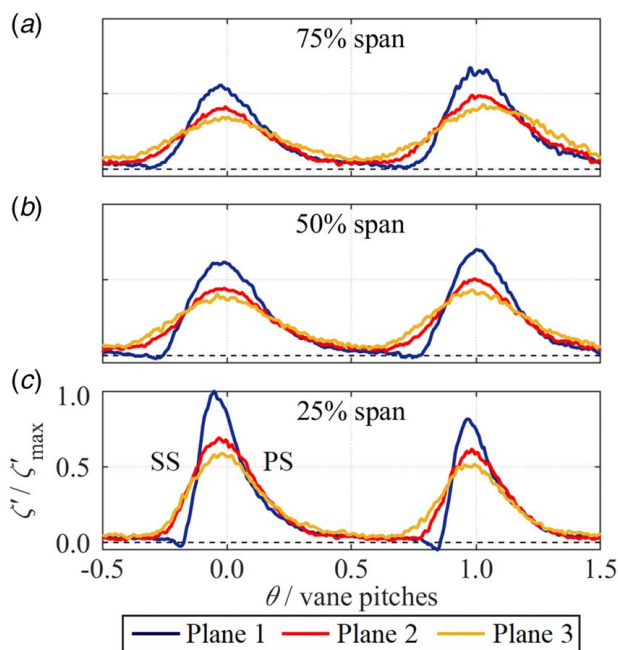


Fig. 12 Circumferential profiles of ζ' extracted from experimental traverse measurements at planes 1–3 at (a) 75% span, (b) 50% span, and (c) 25% span

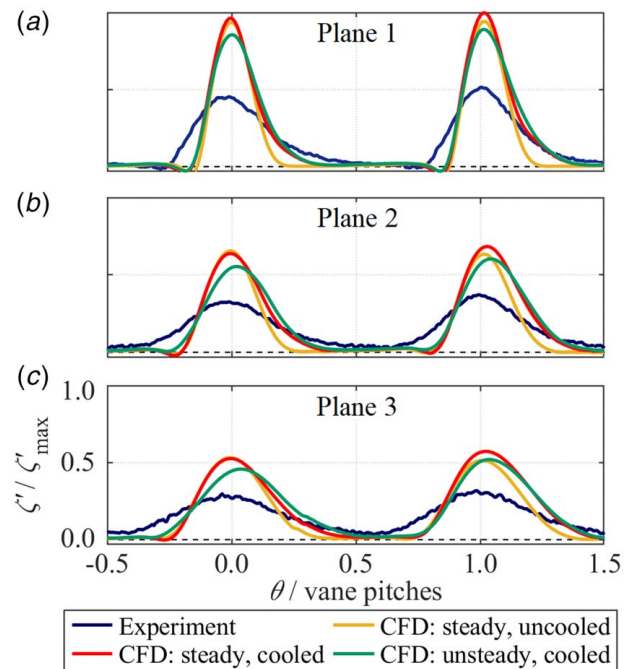


Fig. 13 Comparison of midspan circumferential profiles of ζ' between experiment and three CFD methods at: (a) plane 1, (b) plane (2), and (c) plane 3

around 14%), where the presence of late PS film cooling rows widens the wake by increasing the accumulation of low-momentum flow and enhancing the mixing loss. This increases the asymmetry in the profile shape, more closely matching the experiment.

The effect of moving between steady and time-averaged unsteady predictions (both with film cooling) is a small drop in peak loss (approximately 11.5%) and an increase in wake width (by 14.0% at the half-height points). The effect on overall loss coefficient is relatively small, so these are the concomitant effects of enhanced mixing, particularly due to TE vortex shedding. The result is a marginally improved match with the experiment.

Radial Profiles of Local Kinetic Energy Loss Coefficient: Comparison of Experimental Data at Different Axial Planes. We now consider radial profiles of circumferentially mass flux-averaged KE loss coefficient, ζ''' (Eq. (3)). Experimentally measured radial profiles of ζ''' at planes 1, 2, and 3 are compared in Fig. 14. Note that radial profiles we present have no radial averaging or smoothing: each data point represents an individual sweep of the traverse probe.

In the region between 20% and 80% span, the average loss coefficient is fairly constant and relatively similar between the three planes. This region is dominated by 2D profile loss, so this result is expected. Examining this region in more detail, we see small radial fluctuations, particularly noticeable at plane 1. Local minima can be seen at approximately 14%, 28%, 40%, 54%, 70%, and 86% span. The same minima are present in downstream planes, but are more mixed out. These radial locations match the position of the minima in the wake signatures observed in Fig. 10(a). Recall that we noted these features in the local loss coefficient distributions (Fig. 10) align with the internal cooling lands (solid ribs) within the TE slot (see Fig. 9). Loss coefficient minima—indicated by a narrower and shallower wake in the local distribution and a local minimum of ζ''' in the radial profile—occur directly downstream of solid ribs within the TE slot. At these locations, a local deficit of coolant flow is expected, with higher losses between ribs where coolant is injected.

The regions 0–20% span and 80–100% span have contributions from both profile loss and endwall loss. Moving from plane 1 to 3, the loss coefficient in this region increases and the region of deficit expands. At the hub, the mean loss (between 0% and 20% span) increases by +301.6% between planes 1 and 2 and by +34.7%

between planes 2 and 3. The corresponding increases at the case (80–100% span) were +30.3% and +2.4%. These increases can be attributed to both mixing out of secondary kinetic energy (SKE) and endwall boundary layer growth. The particularly strong rise between planes 1 and 2 at the hub is likely dominated by the mixing out of strong secondary flows (e.g., the distinct secondary loss core just outside of the hub boundary layer at ~10% span, corresponding with the hub passage vortex core).

Radial Profiles of Local Kinetic Energy Loss Coefficient: Comparison of Computational Fluid Dynamics and Experimental Data. We now compare radial profiles of circumferentially mass flux-averaged KE loss coefficient, ζ''' , between experiment and CFD. Figure 15 compares experimental and CFD data (three methods) at plane 2. In the range 80–95% span, there is a significant minimum in loss coefficient in all three CFD simulations, not seen in the experimental data (see also Figs. 11(b) and 11(c)). This is associated with radially inward migration of low-momentum secondary flow and wake region flow, an effect that is significantly more pronounced in CFD than in the experiment.

All three CFD methods overpredict the average loss coefficient over the 20%–80% span profile region. The overpredictions with respect to the experimental mean in this region were +2.3%, +22.4%, and +24.9% for the uncooled RANS, cooled RANS, and cooled URANS methods, respectively. That is, ζ''' is slightly overpredicted by uncooled RANS and greatly overpredicted by both the cooled RANS and URANS methods. We infer that approximately 90% of the overprediction in the two cooled CFD methods might be attributed to overprediction of the total pressure loss associated with film cooling. A significant improvement could be likely achieved by replacing the source-terms film cooling model with fully resolved cooling hole geometries (at the cost of computation time). The remaining small differences between experimental data and uncooled RANS are likely caused by a combination of inaccurate predictions of base pressures and boundary layer thicknesses, and overprediction of radial migration (downwash), resulting in the region of very low loss coefficient between 80% and 95% span (profile loss region confined to a smaller radial range, giving a slightly higher average ζ''').

We now examine more closely the secondary radial variation in ζ''' within the profile region (20–80% span). Recall that our local definition of ζ''' —Eq. (3)—does not include the KE of coolant

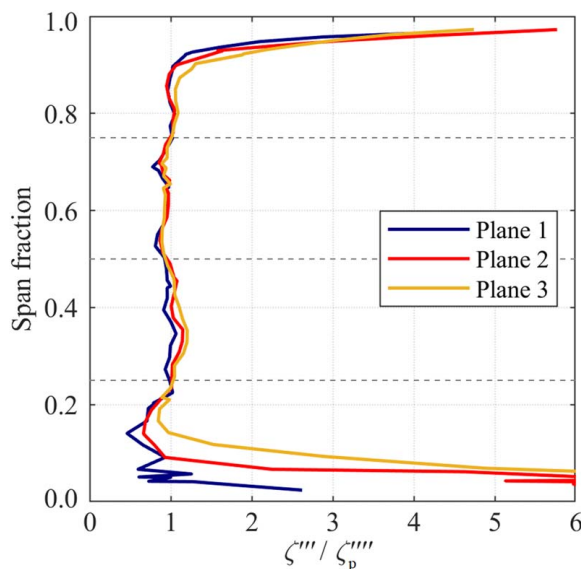


Fig. 14 Experimentally measured radial profiles of circumferentially mass flux-averaged KE loss coefficient, ζ''' , in three axial planes

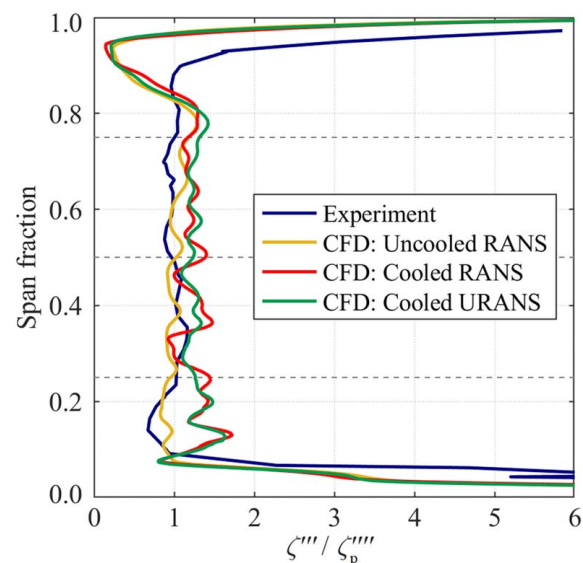


Fig. 15 Radial profiles of circumferentially mass flux-averaged ζ''' for experiment and three CFD methods at plane 2

flow in the denominator (a necessity because local coolant mass fraction is unknown). The consensus in the literature is that, for a KE loss coefficient not accounting for changes in coolant mass flowrate in the denominator, loss coefficient first increases with the introduction of moderate TE coolant flow, before reaching a maximum and then falling as the flowrate becomes large [9,10,42]. The trend in the experimental data (see Fig. 14 and analysis) is for ζ''' minima directly downstream of the solid ribs (lower coolant flowrate) and ζ''' maxima downstream of the open TE (higher coolant flowrate). This suggests that in the experiment, the local coolant mass flowrates are distributed on the rising part of the curve—before the point of maximum loss (for the given geometry).

Looking now at the uncooled RANS profile, we see an opposing trend, with ζ''' maxima directly downstream of the solid ribs at 14%, 27%, 39%, 52%, 66%, and 79% span (lower coolant flowrate) and ζ''' minima downstream of the open TE (higher coolant flowrate). This suggests that the CFD-predicted local coolant mass flowrate downstream of the open TE is located on the falling part of the curve, beyond the maximum point (similar overall mass flowrate, but locally higher due to undermixing as it emerges from the slot). The results for the cooled RANS and cooled URANS methods have a more ambiguous trend. The TE slot radial signature is conflated with distinct ζ''' maxima associated with individual film rows (these being significantly undermixed with respect to the experiment). URANS slightly damps out the radial variation due to the enhanced mixing induced by vortex shedding close to the TE.

Circumferential Distributions of Whirl Angle. In Fig. 16, we compare circumferential profiles whirl angle, β , at midspan in planes 1, 2, and 3 between experiment and all three CFD methods. Here, β is defined as the angle between the local velocity vector and the axial direction in the axial-circumferential plane. Vertical dashed lines indicate approximate wake center locations.

The profile shapes vary significantly between the three axial planes and between experiment and CFD, but the variation between the CFD methods is small. That is, the result is relatively independent of the fidelity of the method and of film coolant introduction, other than a small (<0.7 deg) local β -reduction to the PS of the wakes, where film concentration is high.

The most striking difference between experiment and CFD is that, in all three planes, the variation in β over the profile is

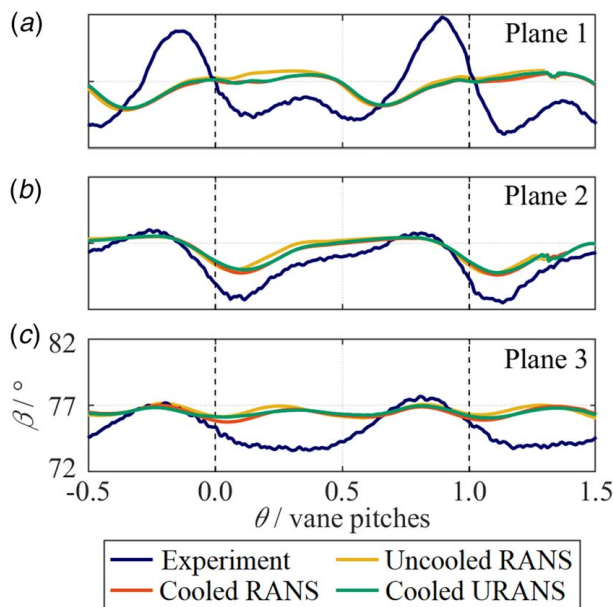


Fig. 16 Circumferential profiles of whirl angle at midspan for experiment and three CFD methods, in three axial planes

greater in the experiment (range of 8.8 deg, 5.5 deg, and 4.1 deg in planes 1, 2, and 3, respectively) than CFD (range of 2.7 deg, 2.7 deg, and 0.9 deg in planes 1, 2, and 3, respectively). This difference in trend (as opposed to absolute magnitude) appears to be dominated by the failure of CFD to adequately predict the peak in β to the SS of the TEs ($\theta \approx -0.2$ and 0.8). This is thought to be due to overprediction of shock–boundary layer interaction causing the SS boundary layer to separate upstream of the TE, leading to local underturning on the SS.

We now consider the different circumferential β distributions between the three planes. The profile in plane 2 has the expected shape: a steep whirl angle gradient from a maximum on the SS to a minimum on the PS (corresponding to the difference in TE metal angles) and a shallow β -gradient across the passage.

The circumferential profile in plane 1 has an additional secondary minimum near the passage center ($\theta = 0.55$) instead of a continuous, shallow gradient. This is caused by a local static pressure maximum, which diffuses the flow and turns it toward the axial (mildly subsonic flow turning into greater area), i.e., toward lower β . This effect is analyzed in detail in Ref. [43]. The same excursion in the static pressure field intersects plane 2 near the wake center and is responsible (in combination with mixing) for the reduction in whirl angle at the SS peak (by -2.8 deg) and at the PS minimum (by -1.5 deg) between planes 1 and 2.

Radial Distributions of Whirl Angle. Figures 17(a) and 17(b) show radial profiles of circumferentially mass flux-averaged β , in the axial planes 1–3, for experiment and cooled URANS, respectively. The general shape of the radial profile was closely matched between experiment and CFD, showing a gradual increase in mean turning angle moving radially outward between 17% and 66% span and an approximately constant value between 66% and 93% span. Below 10% span, all profiles have the expected characteristic overturning of the endwall boundary layer and underturning of the secondary flow just outside the boundary layer. In experiment, the underturned secondary flow was only visible in plane 1, before being overwhelmed by the overturned boundary layer in planes 2 and 3. CFD shows some underturning at the location of the secondary flow in all three planes due to the lower rate of the boundary layer growth.

The experimental data show a small reduction in mean turning angle from plane 1 to 3 over most of span. The average changes

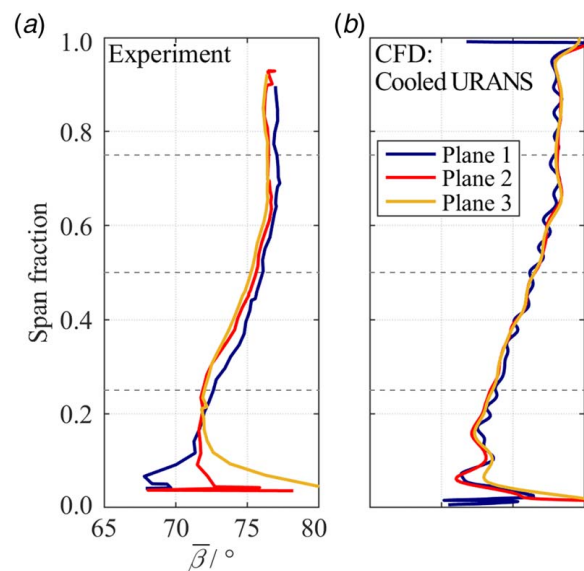


Fig. 17 Radial profiles of circumferentially mass flux-averaged flow turning angle, β , for (a) experiment and (b) cooled URANS, in three axial planes

in $\bar{\beta}$ over the range 20–80% span were -0.45 deg between planes 1 and 2 and -0.15 deg between planes 2 and 3. In contrast, cooled URANS show almost no change in whirl angle between the three axial planes (<0.10 deg).

The absolute values of circumferential mean whirl angle are slightly overpredicted in CFD. The average offsets between experiment and each of the three CFD methods, evaluated over 20–80% span, were $+0.74$ deg, $+0.66$ deg, and $+0.70$ deg for uncooled RANS, cooled RANS, and cooled URANS, respectively. These absolute offsets are considered to be remarkably small: well within the bias error of the probe, which is estimated as ± 1.72 deg. This error includes calibration method errors (matrix inversion, etc.), instrumentation chains in both the calibration and the unknown-flow environment, rotational position errors, etc. For completeness, we note that the change in average whirl angle between the three CFD methods (not shown) was extremely small (within 0.09 deg over most of the span).

Method for Characterizing Wakes. The tendency of CFD methods to significantly overpredict peak loss coefficient and underpredict wake width gives poorly defined inlet conditions to the following rotor row. The implications of this for design are significant, in terms of both the performance penalty due to unsteady inlet flow (off-design incidence angles) and the optimization of the rotor cooling system. By understanding and quantifying this, we aim to provide better guidelines for CFD characterization and turbine design.

To do this, we now characterize a *mean profile* obtained by averaging a series of underlying profiles over a 10% span range. In experiments, the underlying profiles are individual passes of the traverse probe (see Fig. 5) within the averaging range, and in CFD, they are rows of a uniformly spaced grid within the averaging range. The underlying and mean profiles are shown in Fig. 18, taking an example from cooled URANS CFD. We see that the main difference between underlying profiles is in the width of the distribution on the PS of the peak, caused by radial variations in local film coolant concentration. We characterize the wake by peak height, peak width (circumferential range over which ζ' exceeds 50% of the peak height, indicated by solid black lines), and circumferential-average value (dashed black line). The axial variation of each of these parameters is now examined in turn.

Variation in Wake Peak Height With Axial Distance. Figure 19 shows axial trends in the peak value of ζ' at 25% (downward-pointing triangles), 50% (circles), and 75% span (upward-pointing triangles) for experiment, uncooled RANS, and cooled URANS, respectively. As expected, all of the data follow a quasi-exponential decay. As observed previously, the CFD methods predict higher peak loss coefficient than in experiment

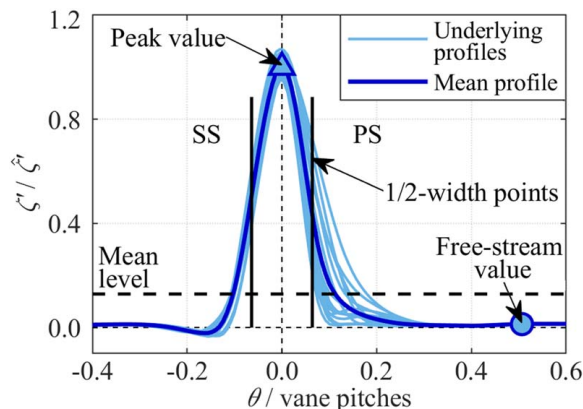


Fig. 18 Circumferential variation of local KE loss coefficient in a 10% span range around midspan

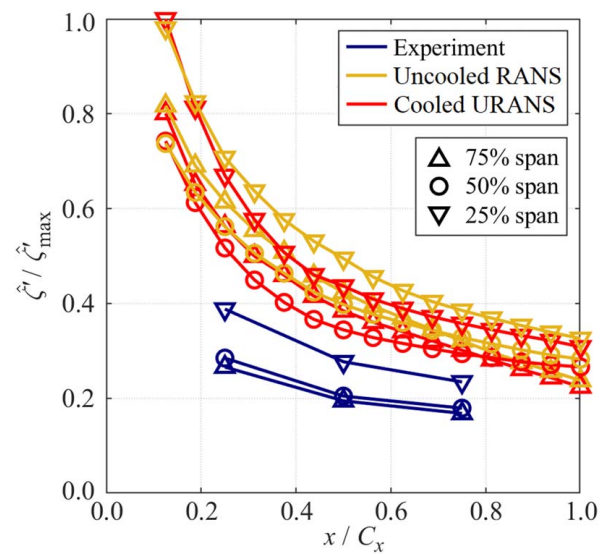


Fig. 19 Axial trends in peak KE loss coefficient, ζ' , at three spanwise locations, for experiment and two CFD methods

due to both the underprediction of mixing and the overprediction of overall loss. Peak ζ' is higher close to the hub (see also Fig. 12 and analysis), with the trends at 50% and 75% span being similar. The greater peak loss coefficient at 25% span is primarily driven by vane sweep and turning profile differences with radius, which lead to different streamline path lengths between the TE and the measurement planes at the three span locations.

Considering both the *spanwise-local* axial distance between the TE and each measurement plane, x' , and the mean turning angle at each span location, $\bar{\beta}$, we calculate the actual streamwise path length, d , between the local TE and the measurement plane, for each of 25%, 50%, and 75% span, as $d = x' \cos \bar{\beta}$. The results for each of planes 1, 2, and 3 are shown in Fig. 20. We see that the streamwise path length is greatest at 60% span and reduces moving away in either direction, becoming particularly small near to the hub.

In Fig. 21, we then replot the data in Fig. 19 as a function of d/C_x (in place of x/C_x). The collapse of the data at the three spanwise locations on to a single trend for each of experiment, uncooled RANS and cooled URANS, is quite compelling. Best-fit curves (least-squares method) give $d^{-0.45}$ for uncooled RANS and order $d^{-0.90}$ for cooled URANS (steeper initial decay due to the enhanced mixing close to the TE associated with TE vortex shedding). These are close to the $d^{-0.50}$ characteristic observed by previous studies (e.g., Refs. [44,45]). Experimental data are well fitted

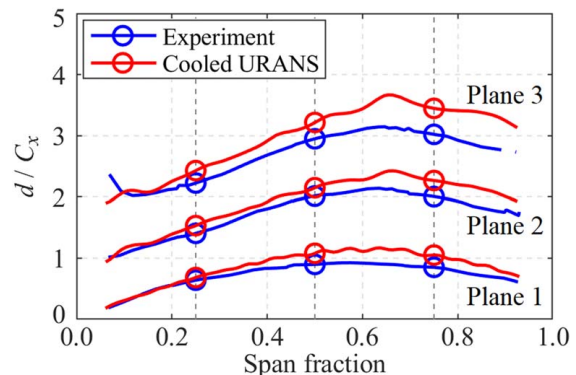


Fig. 20 Spanwise profiles of streamwise path length, d , between the local TE and each of planes 1, 2, and 3

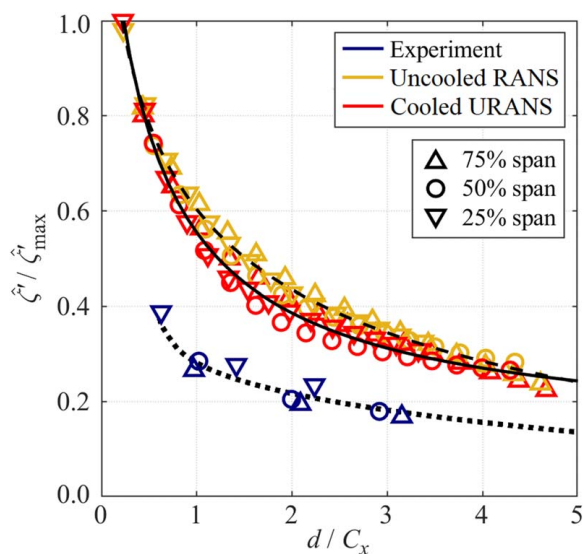


Fig. 21 Trends in peak KE loss coefficient, ζ'' , at three spanwise locations, with local streamwise path length

with a $d^{-0.50}$ characteristic (R^2 equal to 0.94), but the data are too sparse to estimate a meaningful best-fit decay rate.

The good collapse of these data suggests that, even for vanes of moderate sweep, care should be taken when interpreting data at a single axial plane. The collapse also provides a basis for a model of peak loss coefficient decay based on the local streamwise path length.

Streamwise Development of Wake Width. Figure 22 shows axial trends of wake width, w , at 25%, 50%, and 75% span for experiment, uncooled RANS, and cooled URANS as a function of local streamwise path length, d/C_x . In both experimental and CFD trends, the wake width increases monotonically with streamwise distance as the wakes mix out. With respect to experiment, the CFD simulations are undermixed, and the absolute wake width at an equivalent streamwise path length is lower. For all of the data, the mixing rate is highest at the case and lowest at the hub.

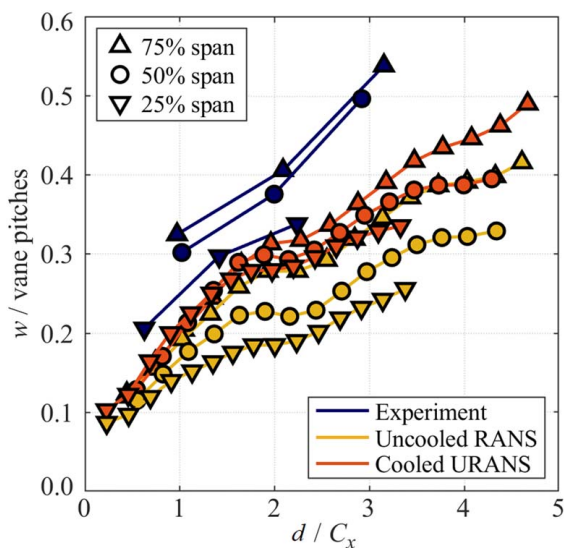


Fig. 22 Trends in wake width, w , at three spanwise locations, as a function of local streamwise path length

There is a modulation in the gradient of wake width with streamwise distance, with regions of reduced gradient at $d/C_x \approx 2.0$ and $d/C_x \approx 4.0$. This is clearly seen in both CFD methods and supported by the experimental data despite its low streamwise resolution. The modulation is caused by periodic streamwise pressure gradients, which the flow passes through as it develops downstream of the cascade. A narrow region of high pressure extends almost axially downstream of each TE, resulting in periodic diffusion (enhanced rate of wake spreading) and acceleration (reduced rate of wake spreading) of the flow, in phase with the vane pitch spacing (approximately every $d/C_x \approx 2.0$ in the streamwise direction). The same effect is responsible for influencing the whirl angle profiles in different axial planes (Fig. 16 and associated discussion). This effect is discussed in detail in Ref. [43] and is in accord with the results of Thomas and Liu [45] who studied the response of turbulent wakes to different streamwise pressure gradients.

For completeness, we note that trends in wake width as a function of axial distance from the midspan TE (x/C_x , not presented) are similar, but with greater variation between the different spanwise locations.

Streamwise Development of Circumferential Mean Kinetic Energy Loss Coefficient. Figure 23 plots circumferentially mass flux-averaged KE loss coefficient at 25%, 50%, and 75% of span as a function of streamwise distance, d/C_x . The data are averaged over a 10% span region centered on the relevant spanwise location. Presented in this way, both the experimental and cooled URANS data have reasonably good agreement between spanwise locations in their respective trends. In contrast, uncooled RANS simulations show significantly higher mean loss coefficient at 75% span than other span locations. For $0 < d/C_x < 3$, all of the characteristics have very similar trends with a gradual increase in ζ''' with streamwise distance. This is expected on the basis of gradual mixing out of SKE. The cooled URANS simulations overpredict the average loss coefficient by approximately +27.0% with respect to the experimental data.

Explaining secondary variations in the trends is more complex and influenced by the modulation of wake mixing rate under the influence of the periodic streamwise pressure gradient (see discussion around Fig. 22). We can see, for example, that both the uncooled RANS and cooled URANS trends at 50% span reach a plateau at around $d/C_x = 2$, before increasing again further downstream. A second effect is radially inward migration of lower

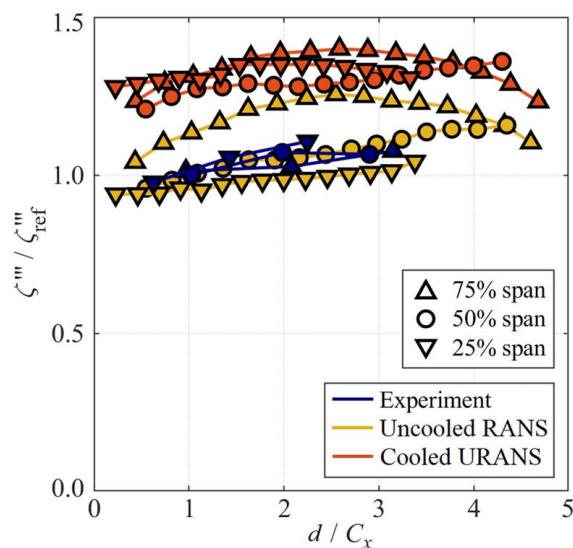


Fig. 23 Trends in mass flux-averaged KE loss coefficient, ζ''' , at three spanwise locations as a function of local streamwise path length

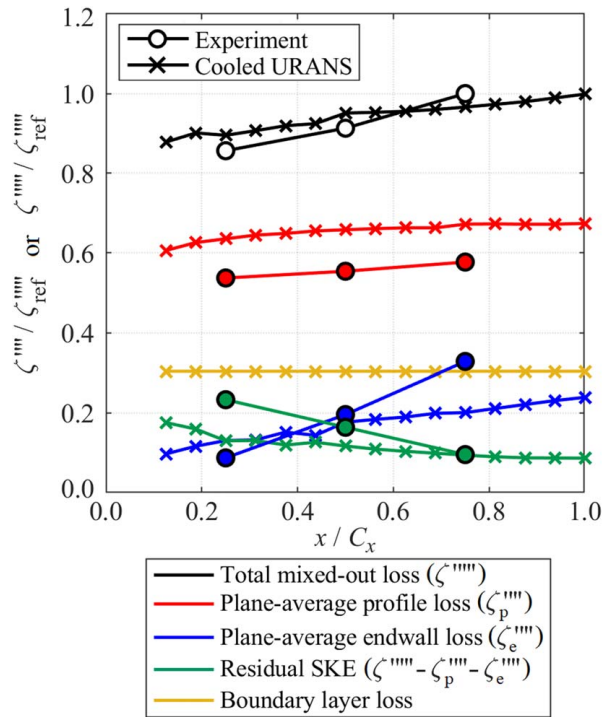


Fig. 24 Axial trends of plane-averaged KE loss coefficient, ζ'''' , and mixed-out KE loss coefficient, ζ''''' , for experiment and cooled URANS

momentum secondary and coolant flows, which changes the composition of the flow being averaged with increasing streamwise distance. As an example of this, looking at 75% span data, we see that both CFD simulations show a sharp reduction in KE loss coefficient for $d/C_x > 3$. This is attributed to the region of very low loss coefficient predicted by CFD near the case (see Figs. 10 and 15) starting to encroach on the 75% span averaging region.

The average KE loss coefficient evaluated at a specific spanwise location is clearly sensitive to a number of factors and requires careful interpretation.

Axial Development of Plane-Averaged and Mixed-Out Kinetic Energy Loss Coefficients. We now consider the axial development of plane-averaged loss coefficient, ζ'''' (Eq. (4)), and mixed-out loss coefficient, ζ''''' (Eq. (5)), for experimental data and cooled URANS. These data are presented in Fig. 24, normalized with respect to the experimental mixed-out loss coefficient in plane 3.

Plane-averaged loss coefficient is further separated into *profile* and *endwall* components (common practice, e.g., Ref. [3]) using integration regions that distinguish the two: a detailed explanation of the method is given in Appendix B. In line with arguments presented earlier in this article, we refer to the difference between mixed-out loss coefficient and plane-averaged loss coefficient as *residual SKE*. This is also shown in the figure. Finally, for

cooled URANS simulations, the KE loss due to viscous dissipation in the vane surface boundary layers is also plotted. This is estimated from velocity profiles extracted at midspan, assuming uniform thickness across the span, using the method of Ref. [44]. The remaining difference between profile plane-averaged loss coefficient and boundary layer loss can be attributed to TE and mixing losses upstream of the traverse plane. Table 2 summarizes the magnitudes of each loss component in each of planes 1–3, expressed as percentages of the total mixed-out loss coefficient in that plane.

The following observations are drawn:

- (1) Axial gradients of loss coefficient are broadly as expected. Plane-averaged profile loss coefficient increases slowly in the downstream direction, as SKE is gradually converted to total pressure loss. Plane-averaged endwall loss coefficient increases more rapidly with axial distance due to both boundary layer growth and concentration of SKE in the endwall flow. Residual SKE falls in the downstream direction as it mixes out. There is a positive axial gradient of total mixed-out loss coefficient, explained by endwall boundary layer growth.
- (2) Cooled URANS overpredicts the absolute plane-averaged profile loss coefficient with respect to experiment by an average (between planes 1, 2, and 3) of 17.9%. The difference in the absolute value of profile loss coefficient is primarily attributed to overprediction of the total pressure loss associated with film cooling. The difference between the uncooled and cooled CFD results indicates that this accounts for approximately 90% of the overprediction of absolute loss coefficient. Inaccurate prediction of base pressures and boundary layer thicknesses and overprediction of the radial downwash effect of lower momentum flow (including coolant flow) are likely smaller contributing effects.
- (3) There is good agreement between experiment and cooled URANS for the total mixed-out loss coefficient. The average (across data in planes 1, 2, and 3) discrepancy between experimental and numerical data is 4.0%. This result is somewhat contrary to expectation as the underprediction of mixing rates by CFD would lead us to expect greater residual SKE in CFD than in experiment. Close to the TE (e.g., in plane 1), both plane-averaged profile and endwall loss coefficients are overpredicted by URANS. The good agreement in total mixed-out loss coefficient arises from a higher residual SKE in experiment compared to CFD. This could be potentially explained by the greater whirl angle variation observed in the experimental data compared to CFD (see Fig. 16). This may provide the experimental data with an additional mixing loss mechanism. Further downstream (e.g., in plane 3), URANS overpredicts plane-averaged profile loss coefficient but significantly underpredicts plane-averaged endwall loss coefficient (due to underpredicting the boundary layer growth rate on the exit duct endwalls), while the residual SKE is identical. The result closely matches with the total mixed-out loss coefficient. When comparing results between experiment and CFD, the use of mixed-out loss coefficients is therefore strongly recommended.

Table 2 Summary of percentage contributions to mixed-out KE loss coefficient for experiment and cooled URANS in planes 1–3

Loss component	ζ''''' (%) at plane 1 ($x/C_x = 0.25$)		ζ''''' (%) at plane 2 ($x/C_x = 0.50$)		ζ''''' (%) at plane 3 ($x/C_x = 0.75$)	
	Experiment	Cooled URANS	Experiment	Cooled URANS	Experiment	Cooled URANS
Plane-averaged profile loss	62.7%	71.0%	60.7%	69.2%	57.7%	69.6%
Boundary layer loss	—	33.9%	—	31.9%	—	31.4%
Plane-averaged endwall loss	10.1%	14.5%	21.4%	18.5%	32.8%	20.7%
Residual SKE	27.2%	14.5%	17.9%	12.2%	9.5%	9.7%

- (4) The axial gradients of plane-averaged profile loss coefficient and total mixed-out loss coefficient were reasonably matched between experiment and CFD over most of the range. Plane-averaged profile loss coefficient increased between planes 1 and 3 by +7.4% in experiment and by +5.8% in cooled URANS. Total mixed-out loss coefficient increased between planes 1 and 2 by +6.6% in experiment and by +6.2% in cooled URANS. Between planes 2 and 3, however, the rise measured in the experiment (+9.5%) was greater than that predicted by CFD (+1.6%) because of significant underprediction of endwall boundary layer growth.
- (5) The gradient of plane-averaged endwall loss coefficient was significantly underpredicted by CFD (underprediction of the rate of endwall boundary layer growth). Plane-averaged endwall loss coefficient increased between planes 1 and 3 by a factor of 3.78 in experiment, compared to 1.54 in cooled URANS.
- (6) Boundary layer loss (vane surface boundary layers in the profile loss region) is estimated to account for 45.1% of the CFD-predicted plane-averaged profile loss coefficient in plane 3, and 31.4% of the mixed-out loss coefficient.

Sensitivity of Loss Coefficient to Exit Mach Number

All of the data presented so far has been at a common, fixed vane exit Mach number condition $M_2 = 0.97$. We now consider the effect of varying the M_2 condition. Experimental tests were conducted in the ECAT facility operating in blowdown mode (as described in the earlier section). Corresponding numerical simulations were performed at five distinct exit Mach numbers (in the range $0.63 \leq M_2 \leq 1.11$) by varying the downstream static pressure boundary condition. Only cooled RANS simulations were performed at the off-design Mach number conditions to reduce computational time.

Circumferential profiles of ζ' in plane 1 at midspan are plotted in Figs. 25(a) and 25(b) for experiment and cooled RANS, respectively, at the five distinct M_2 conditions. All of the data are normalized with respect to the maximum value of ζ' at $M_2 = 0.97$. We can see that increasing M_2 has two primary effects. First, the peak loss coefficient in the wake center gradually reduces, and second, the wake width gradually reduces mainly due to a significant decrease in loss coefficient to the PS of the peak.

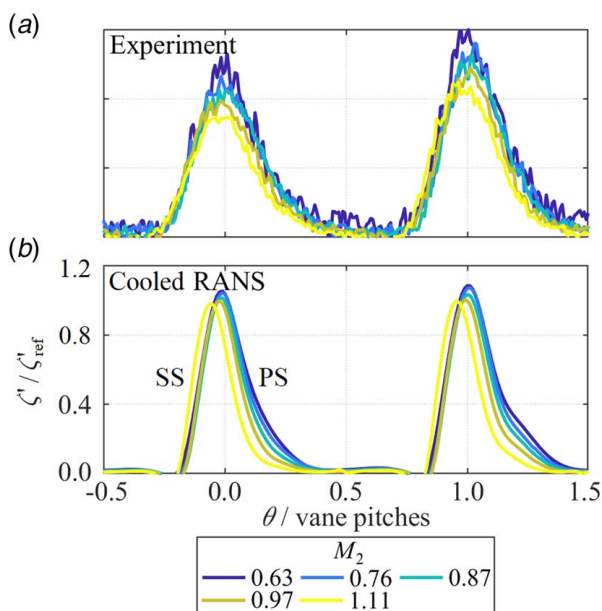


Fig. 25 Circumferential profiles of ζ' at midspan in plane 1, at five different vane exit Mach number conditions

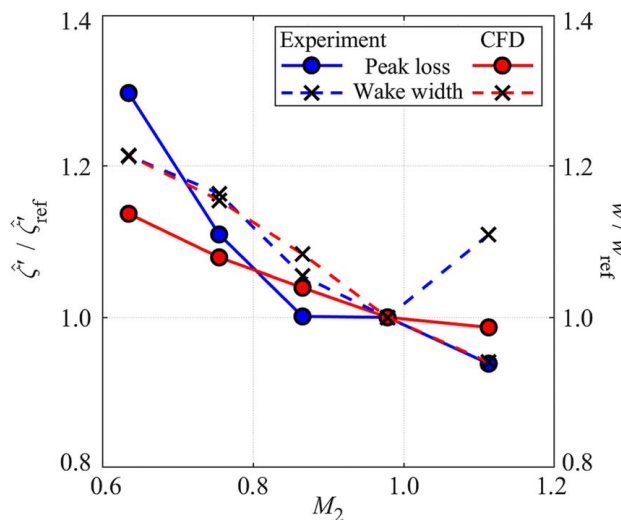


Fig. 26 Midspan trends in peak loss coefficient and wake width, with exit Mach number

In Fig. 26, we plot peak loss coefficient and wake width at midspan as functions of M_2 . All of the data are normalized with respect to the values at $M_2 = 0.97$. In both experiment and CFD, peak loss coefficient falls with increasing M_2 . CFD underpredicts the gradient by approximately 54%. The wake width follows almost the same trend in experiment and CFD for $M_2 < 1.0$, dropping by 21.4% between $0.63 \leq M_2 \leq 0.97$. However, while in experiments, there is an abrupt increase in the width of +10.9% for $0.97 \leq M_2 \leq 1.11$, CFD predicts a reduction in width. The change in behavior at the supersonic M_2 condition is caused by the presence of a shockwave just upstream of the SS TE. This accounts for the widening of the wake profiles in Fig. 25 to the SS of the peaks (sudden late SS diffusion causing rapid boundary layer growth). We further interrogate the difference between the experimental and CFD cases by comparing average loss coefficient values.

Figure 27 compares trends in circumferentially mass flow-averaged KE loss coefficient, ζ''' (Eq. (3)) with M_2 between experiment and cooled RANS, at midspan in plane 3. The experimental data represent an average over two vane pitches and over a thin radial strip around midspan (single pass of the traverse probe, see Fig. 6). Each numerical data point represents an average over two vane pitches and $\pm 5\%$ span around midspan. All of the data in Fig. 27 are normalized with respect to the experimentally-measured loss coefficient at $M_2 = 0.97$.

For $M_2 < 1.0$, both experiment and CFD show an almost linear fall in ζ''' with increasing M_2 . Between $0.63 < M_2 < 0.97$, ζ''' fell by -23.8% in experiment, compared to -27.0% in CFD. For $M_2 > 1.0$, while the numerical trend deviates only marginally from the linear relationship (slightly shallower gradient), the experimental trend increased by +6.2% between $0.97 \leq M_2 \leq 1.11$. The difference in ζ''' between the experiment and cooled RANS at $M_2 = 1.11$ was only 15.5% compared to an average of 40.5% across the four subsonic conditions.

The CFD-predicted trend in mixed-out loss coefficient does show an increase between $0.97 < M_2 < 1.11$, but by only +2.2%. That is, the increased loss coefficient observed in the experimental data at $M_2 = 1.11$ was also present in CFD but to a lesser degree and only when the flow was fully mixed-out. Based on this evidence, the difference between experimental and cooled RANS data is thought to be caused by two effects. First, the shockwave at the SS TE was somewhat poorly resolved in the CFD result and was therefore “smeared out” to give an adverse pressure gradient rather than a sharp discontinuity. This explains why most of the additional loss coefficient associated with the shock is only seen in the CFD data when the flow is fully mixed out (adverse pressure gradient increases the rate of shear in regions of velocity gradient at the edge of the wake). Second, the

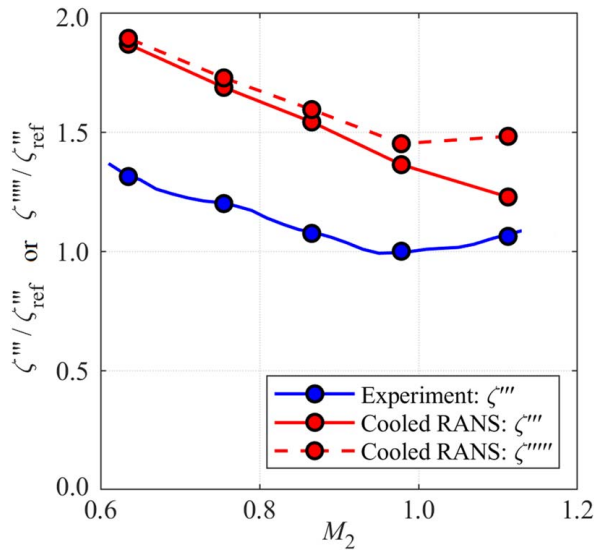


Fig. 27 Circumferentially mass-averaged KE loss coefficient, ζ''' , at midspan in plane 3, as a function of M_2

shockwave in the experimental case may be moving unsteadily. Such an unsteady effect would increase the mixing of the wake profile close to the TE for approximately the same level of overall (mixed-out) loss coefficient. Unsteady movement of the shock would not be expected to be predicted by steady RANS, but may contribute to the smearing out of the shock.

Summary and Conclusions

In this article, we have presented high-fidelity experimental traverse data downstream of an annular cascade of engine component HP turbine NGVs in three axial planes. The data address a gap in the literature for detailed aerodynamic traverse measurements downstream of actual engine parts complete with film and TE cooling flows. They also provide an important benchmark for high-TRL numerical predictions of HP NGV aerodynamic performance. The data have been compared with CFD models at a range of fidelity levels.

All of the CFD models (steady and unsteady, excluding and including surface film cooling) underpredict the rate of mixing out of the nonuniform exit flow field and significantly overpredict the profile loss coefficient (by an average of 17.9%) determined in a given axial plane. The overprediction of profile loss coefficient is primarily attributed to overprediction of the total pressure loss associated with the mixing of surface film cooling. Fully resolving the film cooling holes, in place of a source-terms model, would likely improve the quality of prediction. Inaccurate prediction of base pressures and boundary layer thicknesses and overprediction of the radial migration effect of lower momentum flow (including coolant flow) are smaller contributing effects.

The agreement between experiment and CFD for mixed-out loss coefficient was significantly better than for plane-averaged loss coefficient (average difference of 4.0%, compared with 17.9%). The improved comparison arises because the combined discrepancy in the plane-averaged endwall loss coefficient (underpredicted due to underprediction of the endwall boundary layer growth rate) and the mixing loss coefficient (associated with the mixing out of residual SKE in the flow) is approximately equal in size but opposite in sign to the discrepancy (overprediction) in plane-averaged profile loss coefficient. When comparing results between experiment and CFD, the use of mixed-out loss coefficients is therefore strongly recommended.

The local distributions of loss coefficient downstream of the NGV cascade measured in experiments and predicted by CFD

were also examined in detail, and from this, the key conclusions were presented as follows:

- (1) The experimental wake profile had a distinctive radial non-uniformity in local loss coefficient caused by the presence of internal rib cooling features within the TE slot. This was a significant effect and the sort that would be difficult to detect without testing engine components. CFD methods failed to reproduce the deviations in the radial loss coefficient trend. We propose a mechanism that could explain the discrepancy, but feel this warrants further investigation.
- (2) Significant differences in circumferential local loss coefficient distributions were observed between different radial sections in the same axial plane. These differences arise because of radial variations in lean, sweep, and turning angle, which cause the streamwise path length between the TE and a specific axial plane to vary with radial height. A corollary of this radial variation was that axial trends in both peak local loss coefficient and wake width measured at different radial heights did not collapse to a common trend when presented in terms of axial distance. However, when presented as functions of streamwise path length the collapse to a common characteristic was compelling. This illustrates that significant care must be taken when interpreting data measured downstream of real vane geometries. The data also provide a basis for a model of wake profile decay based on local streamwise path length. This is an extremely important outcome for predicting thermal and aerodynamic rotor forcing effects.
- (3) The sensitivity of midspan loss coefficient to exit Mach number was examined. In the subsonic regime, increasing exit Mach number reduced both the peak local loss coefficient and the wake width, producing a drop in average loss coefficient. An increase in loss coefficient was observed when Mach number exceeded unity, associated with the presence of a shockwave at the SS TE.

Acknowledgment

The support of Rolls-Royce plc is gratefully acknowledged.

Conflict of Interest

There are no conflicts of interest.

Data Availability Statement

The authors attest that all data for this study are included in the paper. Data provided by a third party listed in Acknowledgments.

Nomenclature

d	= path length in streamwise direction, m
h	= static enthalpy, J/kg
p	= static pressure, Pa
r	= radial position, m
s	= static entropy, J/kg/K
v	= velocity, m/s
w	= wake width, m
x	= axial distance, m
M	= Mach number, –
T	= static temperature, K
Y	= stagnation pressure loss coefficient, –
\dot{m}	= mass flowrate, kg/s
$\overline{p_{02}}$	= plane-averaged downstream stagnation pressure, Pa
$\overline{p_2}$	= plane-averaged downstream static pressure, Pa
$\overline{p_{02}^*}$	= mixed-out average downstream stagnation pressure, Pa
$\overline{p_2^*}$	= mixed-out average downstream static pressure, Pa
c_p	= specific heat at constant pressure, J/kg/K
h_0	= stagnation enthalpy, J/kg

p_0 = stagnation pressure, Pa
 p_2 = mean vane exit static pressure, Pa
 M_2 = mean vane exit Mach number, –
 C_x = axial chord length, m
 T_0 = stagnation temperature, K
 x' = local axial distance between TE and axial plane, m
 Re = Reynolds number, –

Greek Symbols

α = flow pitch angle, deg
 β = flow turning (or whirl) angle, deg
 $\bar{\beta}$ = circumferential-averaged whirl angle, deg
 γ = ratio of specific heats, –
 ζ = kinetic energy loss coefficient, –
 ζ' = local kinetic energy loss coefficient, –
 $\hat{\zeta}'$ = peak local kinetic energy loss coefficient, –
 ζ'' = kinetic energy loss coefficient accounting for energy input of coolant flow, –
 ζ''' = circumferential-averaged kinetic energy loss coefficient at a particular radius, –
 ζ'''' = plane-averaged kinetic energy loss coefficient, –
 ζ''''' = mixed-out kinetic energy loss coefficient, –
 η = row efficiency, –
 θ = normalized circumferential distance, vane pitches
 ρ = mass density, kg/m³
 $\chi = (\gamma - 1)/\gamma$

Subscripts

0 = stagnation conditions
 1 = vane inlet condition
 2 = vane exit conditions
 c = coolant stream
 e = endwall
 m = mainstream
 max = maximum value
 p = profile
 ref = reference condition for normalization
 s = isentropic condition

Appendix A: Definitions of Loss Coefficient and Efficiency

The literature is divided on the best way to quantify loss (either local or global) and efficiency. We find the clearest summary of the key issues to be given by Day [46] and Day et al. [47]. The key points are revised here.

Basic Loss Coefficient Definitions. The purpose of an NGV is to supply angular momentum flux to the downstream rotor. The local momentum flux is proportional to the local kinetic energy (KE) per unit volume. This leads to the following practical definition of vane efficiency:

$$\eta = \frac{\text{Actual exit KE}}{\text{Ideal exit KE}} \quad (\text{A1})$$

The actual KE can be measured, but—even for a completely uniform flow—the ideal KE must be defined. One rational choice is the kinetic energy obtained in an isentropic expansion from the inlet total pressure to the exit static pressure. That is,

$$\eta = \frac{v_2^2}{v_{2s}^2} = \frac{h_0 - h_2}{h_0 - h_{2s}} \quad (\text{A2})$$

where v_2 is the measured flow velocity at vane exit, v_{2s} is the *isentropic velocity* at vane exit, and, for an adiabatic nozzle, $h_{01} = h_{02} = h_0$. This is represented on the h - s chart in Fig. 28(a), for a process between inlet conditions p_{01} , p_1 , and exit conditions p_{02} , p_2 .

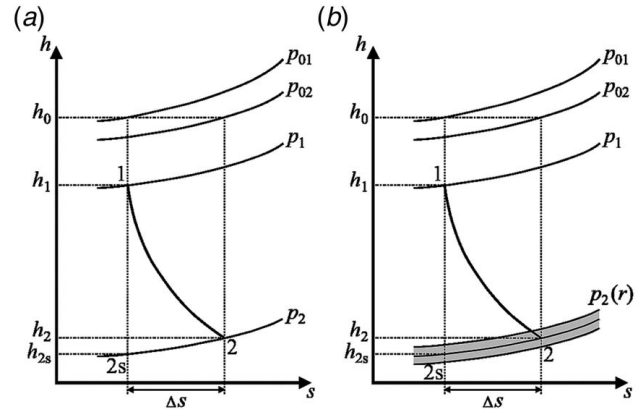


Fig. 28 h - s charts showing the expansion process for (a) uniform exit static pressure and (b) radial profile of exit static pressure

Expressing the efficiency, η , as a kinetic energy loss coefficient, $\zeta = 1 - \eta$, we get

$$\zeta = 1 - \frac{\left(1 - \frac{h_2}{h_0}\right)}{\left(1 - \frac{h_{2s}}{h_0}\right)} \quad (\text{A3})$$

For constant c_p , and recalling the isentropic relation $T_2/T_1 = (p_2/p_1)^\chi$, where $\chi = (\gamma - 1)/\gamma$, this can be cast as follows:

$$\zeta = 1 - \frac{1 - \left(\frac{p_2}{p_{02}}\right)^\chi}{1 - \left(\frac{p_2}{p_{01}}\right)^\chi} \quad (\text{A4})$$

Here, for completeness, we note that in the incompressible limit Eq. (A4) is identical to the total pressure loss coefficient, $Y = (p_{01} - p_{02})/(p_{01} - p_2)$. This is a poor measure of loss in transonic flows as strictly speaking $p_{01} - p_2$ is not proportional to the local KE, because, in general, $p_0 - p \neq 0.5\rho v^2$.

Definitions of Loss Coefficient With Nonuniform Exit Flow.

In most practical cases, even for the case of uniform inlet flow (constant p_{01} and T_{01}), the cascade exit pressures will be nonuniform. The total pressure, p_{02} , will vary on account of nonuniformly distributed loss. The static pressure, p_2 , will vary due to cross-passage pressure gradients and—in the case of annular cascades—the radial pressure gradient required to maintain radial equilibrium. The situation is shown in Fig. 28(b), where the shaded region shows the range of exit static pressures.

In a nonuniform static pressure field (such as downstream of an NGV), there are a number of common loss metrics and representations of those metrics (averaging methods) for loss. Some of these metrics and representations are discussed in Ref. [43], ranging from local distributions, to 1D circumferential-averages and 2D plane-averages at particular locations (primarily used to examine spatial loss variations in the radial, circumferential, or axial directions), to fully mixed-out loss coefficient values. Although mixed-out loss is the most conventional way of presenting overall component performance and while it can be argued that in most turbomachinery situations any residual SKE will eventually manifest as loss (i.e., cannot usefully be used by the following row), it is also true that the flow entering the downstream row is generally only partially mixed (rows relatively close together). Thus, while the mixed-out loss is arguably the most relevant value, it is not necessarily the value manifest at the inlet to the next row.

If the aim is to examine the distribution of kinetic energy loss coefficient at a downstream plane, a *local* kinetic energy loss

coefficient can be defined at every point in the flow by

$$\zeta'(r, \theta) = 1 - \frac{1 - \left(\frac{p_2(r, \theta)}{p_{02}(r, \theta)}\right)^\chi}{1 - \left(\frac{p_2(r, \theta)}{p_{01}}\right)^\chi} \quad (\text{A5})$$

where $p_2(r, \theta)$ and $p_{02}(r, \theta)$ are measured in the plane of interest, and p_{01} , T_{01} are assumed uniform. We use this definition to compare *distributions* of kinetic energy loss.

It is worth making two comments about ζ' . First, now we have a local loss coefficient, it is tempting to define an *overall* loss coefficient—for the vane row—based on an average value of ζ' . Notwithstanding the intricacies of the averaging process (choice of weighting method, whether we average the underlying physical input variables or average ζ' directly, etc.), this is probably a valid approach but is restricted to uniform inlet flows. The complications of nonuniform inlet flows are dealt with in the next section. Second, there is the question of the sensitivity of ζ' to errors in p_2 . This is worth considering because in transonic multihole probe measurements, the static pressure is usually subject to the largest error (Mach number calibration coefficient often has low sensitivity to Mach number in the transonic range, leading to high uncertainty in Mach number and therefore static pressure [48]), and in alternative definitions of loss, the exit static pressure could be determined from hub and case platform measurements rather than probe tip measurements. Figure 29 shows the sensitivity of ζ to both p_{02} and p_2 and indicates that the sensitivity to p_2 is relatively low. A systematic error in p_2 of $\pm 1.0\%$ would result (at a typical ratio $p_{02}/p_{01} = 0.95$) in an error in ζ of $\pm 1.81\%$.

Definitions of Loss Coefficient and Efficiency With Coolant Injection. The simplest possible expression of a cooled vane system is that with uniform p_{01} and T_{01} , and a second inlet stream with coolant plenum total temperature $T_{0c} = T_{01}$, total pressure $p_{0c} > p_{01}$ and of the same specific heat as the mainstream. This represents our system. Even in this case, it is necessary to account for the energy of the coolant flow, which enters the system (defined here as the plenum inlet) at a modestly higher total pressure than the mainstream flow. Naively, we could extend the arguments leading to definition (A4) to include both streams. The result would be a new local KE loss coefficient in which the ideal exit KE is the sum of two ideal expansions:

$$\zeta'' = 1 - \frac{(\dot{m}_m + \dot{m}_c) \left[1 - \left(\frac{p_2}{p_{02}}\right)^\chi \right]}{\dot{m}_m \left[1 - \left(\frac{p_2}{p_{01}}\right)^\chi \right] + \dot{m}_c \left[1 - \left(\frac{p_2}{p_{0c}}\right)^\chi \right]} \quad (\text{A6})$$

where \dot{m}_m and \dot{m}_c are the mainstream and coolant mass flowrates, respectively. All the information required to calculate this local

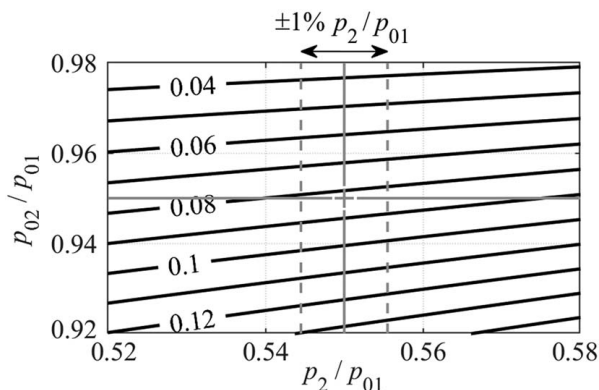


Fig. 29 Sensitivity of ζ to both p_2/p_{01} and p_{02}/p_{01} in typical ranges

parameter is known, and for a uniform—i.e., fully mixed—exit flow, it is well defined. In the case of nonuniform exit flow, however, the problem arises that we additionally require the *local mass flux ratio* (local value of \dot{m}_c/\dot{m}_m) to compute the denominator. In most experiments, not only is this information unavailable, but significant gradients of \dot{m}_c/\dot{m}_m would be expected downstream of the vane (coolant confined primarily to wake regions). The conclusion is that the ideal kinetic energy is not sufficiently defined for the local kinetic energy loss coefficient ζ' —as defined—to have clear meaning. Noting the compromises inherent in the definition, the local KE loss coefficient of Eq. (A5) provides an adequate alternative.

Practical Way Forward for Radial Loss Coefficient Distributions. To establish the radial distribution of loss in a situation with cooling—i.e., a series of circumferential line-averages—the problem arises that the local coolant-to-mainstream mass flux ratio at each radius is generally unknown (unless, in an experiment, by separate temperature measurement, or, in CFD, by—for example—implementation of a scalar tracking method), having both significant concentration in the wakes, but also radial variation. Therefore, it is hard to use a formulation based on Eq. (A6). A practical way forward is to extend Eq. (A5) to a circumferential-average definition by replacing the local value of p_2 with a circumferentially area-averaged static pressure, $\bar{p}_2(r)$, and replacing the local value p_{02} with a circumferentially mass flux-averaged total pressure, $\bar{p}_{02}(r)$. Detailed consideration of the sensitivity to the choice of weighting method for total pressure averaging can be found in Ref. [43]. The circumferential-averaged loss coefficient at a particular radial height then becomes

$$\zeta'''(r) = 1 - \frac{1 - \left(\frac{\bar{p}_2(r)}{\bar{p}_{02}(r)}\right)^\chi}{1 - \left(\frac{\bar{p}_2(r)}{p_{01}}\right)^\chi} \quad (\text{A7})$$

This approach was adopted in the analysis presented in this paper.

Practical Way Forward for Calculation of Plane-Averaged Loss Coefficient. In the case of a plane average, the coolant-to-mainstream mass flux ratio for the *entire plane* is generally known. We can therefore define an average loss coefficient, in which the ideal exit KE is the sum of two terms as in Eq. (A6), by replacing p_2 in Eq. (A1) with a plane area-averaged static pressure, \bar{p}_2 , and replacing p_{02} with a plane mass flux-averaged total pressure, \bar{p}_{02} . The average loss coefficient for a 2D plane becomes

$$\zeta'''' = 1 - \frac{(\dot{m}_m + \dot{m}_c) \left[1 - \left(\frac{\bar{p}_2}{\bar{p}_{02}}\right)^\chi \right]}{\dot{m}_m \left[1 - \left(\frac{\bar{p}_2}{p_{01}}\right)^\chi \right] + \dot{m}_c \left[1 - \left(\frac{\bar{p}_2}{p_{0c}}\right)^\chi \right]} \quad (\text{A8})$$

The flow at the row exit may be considered to have loss *already manifest* as a total pressure deficit, and loss *inevitable* as a result of the mixing out of nonuniformity (secondary kinetic energy). We can consider Eq. (A8) to *count* only the loss already manifest. It is generally accepted, however, that when comparing the *total* row loss between vanes, it is the sum of the two loss terms that should be compared. We refer to this as the *mixed-out loss*, which we now consider.

Practical Way Forward for Calculation of Mixed-Out Loss Coefficient. The process of *mixing-out* requires conservation of mass, momentum, and enthalpy fluxes, in a process of mixing to a well-defined reference flow. The three most commonly used mixing methods are those of Amecke [49,50], Dzung [40], and Main et al. [51,52]. Discussion of the relative merits of these three methods can be found in Refs. [43,51]. The method of Main et al. [51,52], in which the flow is mixed to a radial distribution defined

by a free-vortex condition producing a uniform total pressure and a radial profile of static pressure satisfying radial equilibrium, is considered to be the most physically representative of annular cascade flows. However, the problem arises that the local distribution of coolant mass fraction may be unknown, in which case it must be prescribed to perform the mixing. The alternative method of Dzung [40], in which the flow is mixed to a uniform static pressure at a single swirl-averaged radius (nominal radius at which swirl velocity has its average value), avoids this problem and can be considered as a practical compromise. The method of Dzung is favored by several authors (e.g., Refs. [46,47,53]) and has been shown to produce very similar results to the free-vortex method [43,51].

The outputs of the mixing process are either uniform (i.e., single) values or radial distributions of $\overline{p_2'}$ and $\overline{p_{02}'}$ (and, for completeness, although they are not used in our process, mixed-out values $\overline{\alpha'}$, $\overline{\beta'}$, $\overline{\rho'}$, and $\overline{T_0}$). Here, we use a prime to distinguish average variables resulting from a mixing process from those according to some in-plane weighting (area, mass flow, volume flow, etc.) scheme.

Not only does the Dzung method provide a more rational way of making total loss comparisons between planes but also—happily—the process of swirl-averaged mixing (normally at a midspan radius) to a single static pressure provides a well-defined ideal exit KE (or ideal expansion) in which the problem of mass flux-attribution is resolved. We modify Eq. (A6) by replacing p_2 with $\overline{p_2'}$, and p_{02} with $\overline{p_{02}'}$, to give the mixed-out KE loss coefficient:

$$\zeta'''' = 1 - \frac{(\dot{m}_m + \dot{m}_c) \left[1 - \left(\frac{\overline{p_2'}}{\overline{p_{02}'}} \right)^{\gamma} \right]}{\dot{m}_m \left[1 - \left(\frac{\overline{p_2'}}{\overline{p_{01}'}} \right)^{\gamma} \right] + \dot{m}_c \left[1 - \left(\frac{\overline{p_2'}}{\overline{p_{0c}'}} \right)^{\gamma} \right]} \quad (\text{A9})$$

It is worth noting that in all our experiments and simulations, the coolant-to-mainstream mass flow ratio is fixed, and therefore, the problem of implementing Eq. (A9) reduces to finding the mixed-out values $\overline{p_2'}$ and $\overline{p_{02}'}$.

Appendix B: Methods for Distinguishing Profile and Endwall Loss Coefficients

Figure 30 illustrates three possible integral areas for profile loss (red) and endwall loss (blue) in an example traverse plane (uncooled RANS at plane 1). The local loss coefficient distribution is shown by black contours. The three methods are referred to as methods (a), (b), and (c), respectively.

In method (a), profile and endwall regions are defined by tight boundaries enclosing the identifiable loss regions associated with the wakes, and the hub and case endwall boundary layer flow regions. Free-stream regions are assumed to carry no loss.

In method (b), the integral area for the profile loss region is extended (from method (a)) to include all areas not yet included in an integral. If the loss coefficient in the free-stream were exactly zero, the total (profile + endwall) loss coefficient evaluated by methods (a) and (b) would be identical. In practice, the loss coefficient in free-stream regions is small but non-zero, leading to a small discrepancy between methods (a) and (b).

In method (c), the irregular profile and endwall region integral regions are simplified by using fixed hub and case radial limits. The radial locations of these limits require judgement, but should be set so that most of the endwall loss is included in the endwall integration region. Method (c) is the easiest to implement in practice for obvious reasons.

Loss coefficients determined using each of the three methods (a)–(c) are plotted in Fig. 31 as functions of axial distance for experiment (blue lines) and cooled URANS (red lines). Consider first the profile loss coefficients. A small and consistent offset can be seen between the loss coefficients evaluated from methods (a) and (b). This reflects the loss contribution of the free-stream region (excluded in method (a)). The average difference (over all axial planes) was 5.5% in experiment and 3.5% in CFD. The profile

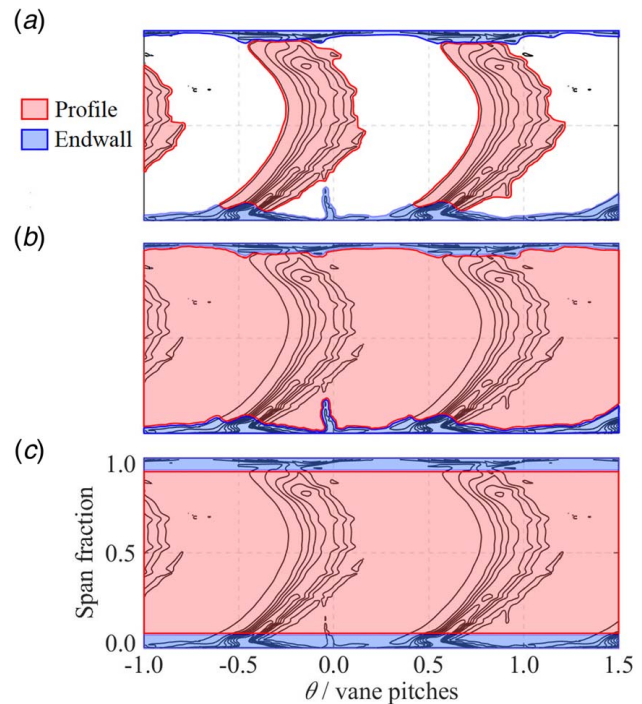


Fig. 30 Illustrations of methods for defining profile and endwall integration regions: (a) tight boundaries around specific features, (b) remaining plane area included in the profile loss integral region, and (c) simple radial limits

loss coefficients evaluated from methods (b) and (c) are nearly identical over most of the axial range, differing by an average of 0.6% in experiment and 1.0% in CFD. Turning to the endwall loss coefficients, we see that the data agree very closely between all three methods for both experimental and CFD data.

The conclusion is that simple radial bounds (method (c)) achieve the same result as the more sophisticated method (b) and that both are advantageous over method (a). In this article, we have used method (c) for distinguishing profile and endwall components of loss coefficient and recommend this as good practice (balance of simplicity and robustness) in most situations.

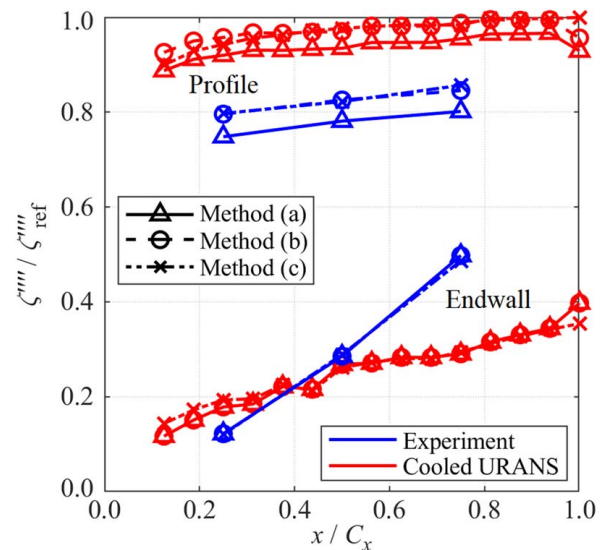


Fig. 31 Axial trends of profile and endwall components of the KE loss coefficient, evaluated using each of methods (a)–(c)

References

- [1] Ainley, D. G., and Mathieson, G. C., 1951, "A Method of Performance Estimation for Axial-Flow Turbines," Aeronautical Research Council, London, UK, Aeronautical Research Council Technical Report No. ARC-R/M-2974, <https://reports.aerade.cranfield.ac.uk/handle/1826/2/3538>
- [2] Carter, A. D. S., 1948, "Three-Dimensional-Flow Theories for Axial Compressors and Turbines," *Proc. Inst. Mech. Eng.*, **159**(1), pp. 255–268.
- [3] Denton, J. D., 1993, "The 1993 IGIT Scholar Lecture: Loss Mechanisms in Turbomachines," *ASME J. Turbomach.*, **115**(4), pp. 621–656.
- [4] Osnaghi, C., Perdicchi, A., Savini, M., Harasgama, P., and Lutum, E., 1997, "The Influence of Film-Cooling on the Aerodynamic Behaviour of a Turbine Nozzle Guide Vane," Proceedings of ASME International Gas Turbine and Aeroengine Congress and Exhibition 1997, Orlando, FL, June 2–5.
- [5] Ardey, S., and Fottner, L., 1998, "A Systematic Experimental Study on the Aerodynamics of Leading Edge Film Cooling on a Large Scale High Pressure Turbine Cascade," Proceedings of ASME International Gas Turbine and Aeroengine Congress and Exhibition 1998, Stockholm, Sweden, June 2–5.
- [6] Day, C. R. B., Oldfield, M. L. G., and Lock, G. D., 1999, "The Influence of Film Cooling on the Efficiency of an Annular Nozzle Guide Vane Cascade," *ASME J. Turbomach.*, **121**(1), pp. 145–151.
- [7] Chappell, J., Ligrani, P., Sreekanth, S., Lucas, T., and Vlasic, E., 2010, "Aerodynamic Performance of Suction-Side Gill Region Film Cooling," *ASME J. Turbomach.*, **132**(3), p. 031020.
- [8] Sieverding, C. H., Arts, T., Dénos, R., and Martelli, F., 1996, "Investigation of the Flow Field Downstream of a Turbine Trailing Edge Cooled Nozzle Guide Vane," *ASME J. Turbomach.*, **118**(2), pp. 291–300.
- [9] Pappu, K. R., and Schobeiri, M. T., 1999, "Optimization of Trailing Edge Ejection Mixing Losses: A Theoretical and Experimental Study," *ASME J. Fluids Eng.*, **121**(1), pp. 118–125.
- [10] Uzol, O., and Camci, C., 2001, "Aerodynamic Loss Characteristics of a Turbine Blade With Trailing Edge Coolant Ejection: Part II—External Aerodynamics, Total Pressure Losses and Predictions," *ASME J. Turbomach.*, **123**(2), pp. 249–257.
- [11] Johnson, J. D., Fiala, N. J., and Ames, F. E., 2009, "Gill Slot Trailing Edge Aerodynamics: Effects of Blowing Rate, Reynolds Number, and External Turbulence on Aerodynamic Losses and Pressure Distribution," *ASME J. Turbomach.*, **131**(1), p. 011016.
- [12] Kapteijn, C., Amecke, J., and Michelassi, V., 1994, "Aerodynamic Performance of a Transonic Turbine Guide Vane With Trailing Edge Coolant Ejection: Part I—Experimental Approach," Proceedings of ASME 1994 International Gas Turbine and Aeroengine Congress and Exposition, Den Haag, Netherlands, 13–16.
- [13] Fiala, N. J., Johnson, J. D., and Ames, F. E., 2010, "Aerodynamics of a Letterbox Trailing Edge: Effects of Blowing Rate, Reynolds Number, and External Turbulence on Aerodynamic Losses and Pressure Distribution," *ASME J. Turbomach.*, **132**(4), p. 041011.
- [14] Melzer, A., 2018, "Aerodynamics of Transonic Turbine Trailing Edges," PhD thesis, University of Cambridge, Cambridge, UK.
- [15] Sauer, H., Müller, R., and Vogeler, K., 2000, "Reduction of Secondary Flow Losses in Turbine Cascades by Leading Edge Modifications at the Endwall," *ASME J. Turbomach.*, **123**(2), pp. 207–213.
- [16] Becz, S., Majewski, M. S., and Langston, L. S., 2004, "An Experimental Investigation of Contoured Leading Edges for Secondary Flow Loss Reduction," Proceedings of ASME Turbo Expo 2004, Vienna, Austria, June 14–17.
- [17] Turgut, ÖH, and Camci, C., 2013, "Influence of Leading Edge Fillet and Nonaxisymmetric Contoured Endwall on Turbine NGV Exit Flow Structure and Interactions With the Rim Seal Flow," Proceedings of ASME Turbo Expo 2013, San Antonio, TX, June 3–7.
- [18] Braüning, W., and Lehthaus, F., 1986, "Investigations of the Effect of Annulus Taper on Transonic Turbine Cascade Flow," *ASME J. Eng. Gas Turbines Power*, **108**(2), pp. 285–292.
- [19] Pullan, G., and Harvey, N. W., 2006, "Influence of Sweep on Axial Flow Turbine Aerodynamics at Midspan," *ASME J. Turbomach.*, **129**(3), pp. 591–598.
- [20] Harrison, S., 1992, "The Influence of Blade Lean on Turbine Losses," *ASME J. Turbomach.*, **114**(1), pp. 184–190.
- [21] Bagshaw, D. A., Ingram, G. L., Gregory-Smith, D. G., and Stokes, M. R., 2005, "An Experimental Study of Reverse Compound Lean in a Linear Turbine Cascade," *Proc. Inst. Mech. Eng. Part A: J. Power Energy*, **219**(6), pp. 443–449.
- [22] Rosic, B., and Xu, L., 2012, "Blade Lean and Shroud Leakage Flows in Low Aspect Ratio Turbines," *ASME J. Turbomach.*, **134**(3), p. 031003.
- [23] Ames, F. E., and Plesniak, M. W., 1997, "The Influence of Large-Scale, High-Intensity Turbulence on Vane Aerodynamic Losses, Wake Growth, and the Exit Turbulence Parameters," *ASME J. Turbomach.*, **119**(2), pp. 182–192.
- [24] Barringer, M. D., Thole, K. A., and Polanka, M. D., 2009, "Effects of Combustor Exit Profiles on Vane Aerodynamic Loading and Heat Transfer in a High Pressure Turbine," *ASME J. Turbomach.*, **131**(2), p. 021008.
- [25] Beard, P. F., Smith, A. D., and Povey, T., 2014, "Effect of Combustor Swirl on Transonic High Pressure Turbine Efficiency," *ASME J. Turbomach.*, **136**(1), p. 011002.
- [26] Binder, A., and Romey, R., 1983, "Secondary Flow Effects and Mixing of the Wake Behind a Turbine Stator," *ASME J. Eng. Gas Turbines Power*, **105**(1), pp. 40–46.
- [27] Sieverding, C. H., Van Hove, W., and Boletis, E., 1984, "Experimental Study of the Three-Dimensional Flow Field in an Annular Turbine Nozzle Guide Vane," *ASME J. Eng. Gas Turbines Power*, **106**(2), pp. 437–444.
- [28] Yamamoto, A., and Yanagi, R., 1985, "Production and Development of Secondary Flows and Losses Within a Three Dimensional Turbine Stator Cascade," Proceedings of ASME 1985 International Gas Turbine Conference and Exhibit, Houston, TX, March 18–21.
- [29] Williamson, R. G., and Moustapha, S. H., 1986, "Annular Cascade Testing of Turbine Nozzles at High Exit Mach Numbers," *ASME J. Fluids Eng.*, **108**(3), pp. 313–320.
- [30] Treiber, M., Abhari, R. S., and Sell, M., 2002, "Flow Physics and Vortex Evolution in Annular Turbine Cascades," Proceedings of ASME Turbo Expo 2002, Amsterdam, Netherlands, June 3–6.
- [31] Yasa, T., Paniagua, G., Fridh, J., and Vogt, D., 2010, "Performance of a Nozzle Guide Vane in Subsonic and Transonic Regimes Tested in an Annular Sector," *Proceedings of ASME Turbo Expo 2010*, Glasgow, UK, June 14–18.
- [32] Sieverding, C. H., 1982, "The Influence of Trailing Edge Ejection on the Base Pressure in Transonic Turbine Cascades," Proceedings of ASME 1982 International Gas Turbine Conference and Exhibit, London, UK, April 18–22.
- [33] Melzer, A. P., and Pullan, G., 2019, "The Role of Vortex Shedding in the Trailing Edge Loss of Transonic Turbine Blades," *ASME J. Turbomach.*, **141**(4), p. 041001.
- [34] Léonard, T., Gicquel, L. Y. M., Gourdain, N., and Duchaine, F., 2015, "Steady/Unsteady Reynolds-Averaged Navier-Stokes and Large Eddy Simulations of a Turbine Blade at High Subsonic Outlet Mach Number," *ASME J. Turbomach.*, **137**(4), p. 041001.
- [35] Kirolos, B., Lubbock, R., Beard, P., Goenaga, F., Rawlinson, A., Janke, E., and Povey, T., 2017, "ECAT: An Engine Component Aerothermal Facility at the University of Oxford," Proceedings of ASME Turbo Expo 2017, Charlotte, NC, June 26–30.
- [36] Burdett, D., Hambidge, C., and Povey, T., 2021, "Analysis of Ultra-Low Uncertainty Gas Turbine Flow Capacity Measurement Techniques," *Proc. Inst. Mech. Eng. Part A: J. Power Energy*, **235**(5), pp. 1053–1079.
- [37] Burdett, D., Lubbock, R., and Povey, T., 2018, "An Impulse Response Technique to Improve the Effective Frequency Response of Pressure Probes," XXIV Biennial Symposium on Measuring Techniques in Turbomachinery, Prague, Czech Republic, Aug. 29–31.
- [38] Hall, B. F., and Povey, T., 2018, "A Practical Model for Pressure Probe System Response Estimation (With Review of Existing Models)," *Meas. Sci. Technol.*, **29**(4), p. 045301.
- [39] Burdett, D., Goenaga, F., and Povey, T., 2021, "Understanding Capacity Sensitivity of Cooled Transonic Nozzle Guide Vanes: A Parametric Experimental and Computational Study of the Impact of Trailing Edge Geometry," *ASME J. Turbomach.*, **143**(5), p. 051001.
- [40] Dzung, L. S., 1971, "Konsistente Mittelwerte in der Theorie der Turbomaschinen für Kompressible Medien," *BBC-Mitt.*, **58**, pp. 485–492.
- [41] Straccia, M., Hofmann, R., and Gümmel, V., 2019, "New Methods for Secondary Flow Phenomena Visualization and Analysis," Proceedings of ASME Turbo Expo 2019, Phoenix, AZ, June 17–21.
- [42] Montis, M., Niehuis, R., Guidi, M., Salvadori, S., Martelli, F., and Stephan, B., 2009, "Experimental and Numerical Investigation on the Influence of Trailing Edge Bleeding on the Aerodynamics of a NGV Cascade," Proceedings of ASME Turbo Expo 2009, Orlando, FL, June 8–12.
- [43] Burdett, D., and Povey, T., 2021, "Analysis of Averaging Methods for Non-Uniform Total Pressure Fields," *ASME J. Turbomach.*, Paper No. TURBO-20-1403.
- [44] Mee, D. J., Baines, N. C., Oldfield, M. L. G., and Dickens, T. E., 1990, "An Examination of the Contributions to Loss on a Transonic Turbine Blade in Cascade," *ASME J. Turbomach.*, **114**(1), pp. 155–162.
- [45] Thomas, F. O., and Liu, X., 2004, "An Experimental Investigation of Symmetric and Asymmetric Turbulent Wake Development in Pressure Gradient," *Phys. Fluids*, **16**(5), pp. 1725–1745.
- [46] Day, C. R. B., 1997, "Aerodynamics of an Annular Film-Cooled Turbine Cascade," DPhil thesis, University of Oxford, Oxford, UK.
- [47] Day, C. R. B., Oldfield, M. L. G., and Lock, G. D., 2000, "Aerodynamic Performance of an Annular Cascade of Film Cooled Nozzle Guide Vanes Under Engine Representative Conditions," *Exper. Fluids*, **29**(2), pp. 117–129.
- [48] Kost, F., 2009, "The Behaviour of Probes in Transonic Flowfields of Turbomachinery," 2009, 8th European Conference on Turbomachinery—Fluid Dynamics and Thermodynamics, Graz, Austria, Mar. 23–27.
- [49] Amecke, J., 1970, "Anwendung der Transsonischen Ähnlichkeitsregel auf die Stromung Durch Ebene Schaufelgitter," *VDI Forschungsh.*, **540**, pp. 16–28.
- [50] Nicholson, J. H., 1981, "Experimental and Theoretical Studies of the Aerodynamic and Thermal Performance of Modern Gas Turbine Blades," DPhil thesis, University of Oxford, Oxford, UK.
- [51] Main, A. J., Oldfield, M. L. G., Lock, G. D., and Jones, T. V., 1997, "Free Vortex Theory for Efficiency Calculations From Annular Cascade Data," *ASME J. Turbomach.*, **119**(2), pp. 247–255.
- [52] Main, A. J., 1994, "Annular Cascade Aerodynamics," DPhil thesis, University of Oxford, Oxford, UK.
- [53] Pianko, M., and Wazelt, F., 1982, "Propulsion and Energetics Panel Working Group 14 on Suitable Averaging Techniques in Non-Uniform Internal Flows," NATO Advisory Group for Aerospace Research and Development, Neuilly-sur-Seine, France, AGARD Advisory Report No. 182.